APPROVAL SHEET

Title of Thesis: Optical and RF beam propagation in turbulent media

Name of Candidate: Nelofar Mosavi
Doctor of Philosophy, 2017

Thesis and Abstract Approved: _____

Curtis R. Menyuk
Professor
Department of Computer Science and
Electrical Engineering

Date Approved: _____

ABSTRACT

Title of Thesis: Optical and RF beam propagation in turbulent media

Nelofar Mosavi, Doctor of Philosophy, 2017

Thesis directed by: Curtis R. Menyuk, Professor
Department of Computer Science and
Electrical Engineering

The optical beam spread and the optical beam quality factor in the presence of both an initial quartic phase aberration and atmospheric turbulence is analyzed. We obtain analytical expressions for both the mean-square beam radius and the beam quality factor using the moment method. We compare these expressions to the results from Monte Carlo simulations, which allows us to mutually validate the theory and the Monte Carlo simulation codes. We also discuss the reason for the discrepancy between the moment method and the classical approach for calculating the ensemble-averaged mean-square beam radius in a turbulent atmosphere that is described by Andrews and Phillips (1) and by Fante (2).

We analyze the first and second-order statistical moments of the fluctuating intensity of a propagating laser beam and the probability density function versus intensity as the beam propagates through a turbulent atmosphere. At the end, we compare our analytical expression and our simulations to field test experimental results, and we find good agreement.

We simulate the propagation of both a partially spatially coherent infra-red (IR) and a visible laser beam through a turbulent atmosphere, and we compare the intensity fluctuations produced in the simulation to the intensity fluctuations that are observed in both maritime and terrestrial environments at the US Naval Academy. We focus on the effect of the level of turbulence and the degree of the beam's spatial coherence on the receiver scintillations, and we compare the probability density function (PDF) of the intensity in

our simulation to the experimental data. We also investigate the effect of optical beam spreading on the coherent and partially coherent laser beams along the propagation path.

Finally, we investigate the evolution of a radio frequency (RF) X-band signal as it propagates through the solar corona turbulence in superior solar conjunction at low Sun-Earth-Probe (SEP) angles. Our analysis of the data that was obtained during several MESSENGER (MErcury Surface, Space ENivornment, GEochmeisty, and Ranging) conjunctions reveals a short term and long term effect. Amplitude scintillation is a smaller effect and is evident on a short time scale. Phase scintillations are stronger, but occur over a longer time duration. We examine different possible phenomena in the solar plasma that could be the source of the different time scales of the amplitude and phase scintillations. We propose a theoretical model in which the amplitude scintillations are due to local fluctuations of the index of refraction that scatter the RF signal. These rapidly varying fluctuations randomly attenuate the signal without affecting its phase. By contrast, we propose a model in which phase fluctuations are due to long ducts in the solar plasma, streaming from the sun, that trap some parts of the RF signal. These ducts act as waveguides, changing the phase velocity of the RF beam as it travels a zigzag path inside a duct. When the radiated wave exits from a duct, its phase is changed with respect to the signal that did not pass through the duct, which can lead to destructive interference and carrier suppression. The trapping of the wave is random in nature and can be either a fast or slow process. The predictions of this model are consistent with observations.

Optical and RF beam propagation in turbulent media

by

Nelofar Mosavi

Thesis submitted to the Faculty of the Graduate School
of the University of Maryland in partial fulfillment
of the requirements for the degree of
Doctor of Philosophy
2017

To my awesome parents, dear husband and sweet son

ACKNOWLEDGMENTS

My most sincere thanks go to my advisor, Dr. Curtis Menyuk, for his guidance and support throughout my PhD journey. His broad knowledge allowed me to explore different avenues in my research and accomplish more than I imagined. He not only introduced me to the wonders and frustrations of scientific research, but also taught me how to think and write like a true researcher, so for that I will always be grateful.

I would like to thank, my advisors and mentors at the Johns Hopkins University Applied Physics Laboratory, Dr. Brian Sequeira and Dr. Bradley Boone. Without their guidance and support, this dissertation would not have been possible.

Part of this project was supported by the Johns Hopkins University Applied Physics Laboratory. I would like to thank Dr. Joseph Suter, Dr. Paul Ostdiek, and Chris Deboy, for their help and support in providing the funds for this project.

I owe special thank to my friends and colleagues, Carl Herrmann, David Jones, Dipak Srinivasan, David Copeland, Bob Wallis, Dr. Brian Marks, Dr. Ray Sova, Dr. Charles Nelson, Dr. NourEddine Raouafi, Dr. Rob Decker, and Ann Darrin.

I would like to thank my parents for their unconditional love and all the sacrifices that they made so that I can pursue my dreams.

Above all, I like to thank my best friend and husband Payam H. Matin for his love, support, and continuous encouragement, as well as my son Arshawn for the joy and warmth that he brings to my heart.

TABLE OF CONTENTS

List of Figures

List of Tables

Chapter 1

Introduction

This dissertation focuses on optical and RF beam propagation in turbulent media. For an optical beam, the turbulent medium is the atmosphere and for an RF beam it is the plasma in the solar corona. This research is broadly comprised of six separate projects. The first three projects focus on optical beam propagation through atmospheric turbulence and possible techniques to reduce scintillations at the receiver. The fourth and fifth projects are concentrated on the data analysis and theoretical study of RF beam propagation through the solar corona during planetary conjunction. Lastly, the turbulence model that was used in the optical studies was implemented for an RF beam to reproduce the amplitude scintillation that was obtained from the data analysis and also to compare the behavior of optical and RF propagation through turbulent media.

First, we obtained an expression for the beam spread in the presence of both quartic beam aberrations and atmospheric turbulence. We evaluated the mutual coherence function using the moments method, and we showed that an exact analytical expression for the ensemble-averaged mean-square beam radius, $\langle \overline{r^2} \rangle$ can be obtained, without first obtaining an expression for the mutual coherence function. We also calculated the beam quality factor, and we showed that this exact expression has the form $M^2_{\text{total}} = 1 + M^2_{\text{ab}} + M^2_{\text{turb}}$, where M^2_{ab} and M^2_{turb} are due to initial aberrations and turbulence respectively, indicating

that the contribution of the turbulence, M^2_{turb}, to the beam quality is strictly additive. We computed the beam radius as a function of the propagation distance. We then compared the analytical results to Monte Carlo simulations and demonstrated agreement. We also compared the Monte Carlo simulation results to the field test data. This work was reported in (3) and (4). Second, we showed that the turbulence contribution $\langle W^2_{\text{turb}} \rangle$ to the beam radius squared, is proportional to distance-cubed (z^3) for all distances and for all refractive-index structure parameters C_n^2, in contrast to a classical result due to Fante (2). The analytical expression has been verified using Monte Carlos simulations. This work was reported in (5). Third, we investigated the possibility of decreasing the receiver scintillations by reducing the spatial coherence of the beam and thereby improving the bit error ratio. We focused on the simulation of a partially spatially coherent laser beam and compared the results with the field test data for both terrestrial and maritime environments. This work was reported in (6).

In the fourth project, my colleagues and I investigated the effect of RF X-band signal as it propagates through the solar corona turbulence in a superior solar conjunction at low Sun-Earth-Probe (SEP) angles. We analyzed recent data obtained during superior solar conjunction of MESSENGER spacecraft at X-band for days 114, 115, 339, 340, and 344 for year 2014 for an SEP angle between 0.7° to 1.84°. Analysis of the data that was obtained over several MESSENGER conjunctions reveals a short term and long term effect. Amplitude scintillation imposed on the carrier signal is a weaker effect and is evident on a short-time scale. Phase scintillation imposed on the carrier is stronger, but occurs over a longer time duration. There is an expected monotonic increase in phase scintillation with decreasing SEP angle (23). However, we find SEP angles where phase estimates are noisier than expected. We have observed two distinct characteristics for the phase scintillation that is induced on the carrier, depending on whether the imposed phase modulation index is about an odd multiple of $\pi/2$ or far removed from it. The proximity of $\pi/2$ is related to

carrier suppression. For example, a carrier suppression of 25 dB occurs within about 0.056 radians (3.2°) of an odd multiple of $\pi/2$ and a 1 dB carrier suppression occurs within 1.1 radians (63.0°). The carrier suppression is significant when the fluctuations in signal-to-noise ratio are noticeably different from those caused by thermal noise alone. Fluctuations of the thermal noise are dependent on solar elongation angle, solar activity, and also receiver noise figure. We have also obtained the phase scintillation spectral density, and we observed two distinct characteristics for it, depending on whether the phase fluctuations suppresses the carrier or not. The phase scintillation spectral density when the carrier is not suppressed is consistent with a Kolmogorov process for which the frequency dependence is proportional to $f^{-8/3}$, and this result is in agreement with prior investigations by Morabito (23) and Imamura (24). However, when the carrier is suppressed, the receiver noise obscures the underlying turbulent process and produces instead an f^{-1} dependence, corresponding to the f^{-1} flicker noise of the receiver. These results have been presented in (7) and (8).

In our fifth project we concentrated on the physical explanation for why the amplitude scintillations and phase scintillations occur on different time scales. The short time scale of one second for the amplitude scintillations is not hard to understand. Solar wind turbulence leads to constant changes in the local index of refraction. Variations in the index of refraction scatter the RF beam and cause the amplitude scintillations (8). The long time scale of hundreds to thousands of seconds for the phase scintillations are harder to explain. We have investigated four phenomena that exist in the solar wind that could potentially explain these long-time phase scintillations. We first investigated the propagation of a radio frequency (RF) wave in the positively and negatively charged clouds of protons and electrons that are approximately a Debye length in size. The difference between the indices of refraction in these clouds will lead to phase variation in the beam wavefront as the RF beam propagates. Second, we investigated the passage of supersonic particles through acoustic waves that

locally change the index of refraction, leading to phase variation in the beam wavefront as the RF beam propagates. Third, we investigated the separation of electrons and protons that are due to inhomogeneous solar magnetic fields. This separation leads to local changes in the indices of refraction and hence phase variations in the beam wavefront as the RF beam propagates. Fourth, we investigated ducts in the solar plasma that trap a part of the RF beam, which leads to a phase difference in the beam wavefront as the RF beam propagates. We concluded that the most probable explanation for the difference in time scales between the amplitude and phase scintillations is the effect of the long ducts.

Lastly, we showed that the same phase screen technique that we used to study optical communications in free space through a turbulent atmosphere can be used to simulate an RF beam as it propagates through the turbulent solar plasma. We reproduced the amplitude scintillations that were observed in our data using a Monte Carlo simulation. Our data and theoretical model were consistent and showed that solar plasma turbulence is consistent with Kolmogorov process, and we confirmed this result with a Monte Carlo simulation.

Chapter 2

Beam spreading in the presence of quartic beam aberrations and atmospheric turbulence

2.1 Analytical Expressions

The classical approach for calculating the ensemble-averaged mean-square beam radius in a turbulent atmosphere is described in Andrews and Phillips (1) and Fante (2). This approach is to find a good analytical approximation for the mutual coherence function and then to carry out an integration over the transverse beam profile. This approach works well with Gaussian beams, but it is not useful for aberrated beams where good analytical approximations for the mutual coherence function are difficult to obtain. Therefore, it is advantageous to use other approaches such as the moment method as described by Feizulin and Kravtsov (9) and by Gbur and Wolf (10). The mean-square beam radius for a beam with a quartic phase aberration in the presence of turbulence had not been studied prior to our work.

The beam radius squared $W^2(z)$ is traditionally defined as twice the mean-square radius, and it can be written as

$$\langle W^2(z)\rangle = 2\langle\overline{r^2}\rangle = 2\frac{\int\int_{-\infty}^{\infty} d^2\mathbf{r}\, r^2\Gamma_2(\mathbf{r},\mathbf{r},z)}{\int\int_{-\infty}^{\infty} d^2\mathbf{r}\,\Gamma_2(\mathbf{r},\mathbf{r},z)}, \tag{2.1}$$

where z is the propagation distance, r is the transverse distance, $\mathbf{r}$ is the corresponding transverse vector, $\overline{r^2}$ is the spatial average of r^2 over the beam profile, and $\langle\overline{r^2}\rangle$ indicates the ensemble average of $\overline{r^2}$ over all turbulence realizations. The mutual coherence function $\Gamma_2(\mathbf{r},\mathbf{r},z)$ [(1), 7.27] can be written as

$$\Gamma_2(\mathbf{r},\mathbf{r},z) = \left(\frac{k}{2\pi z}\right)^2 \int\int_{-\infty}^{\infty} d^2\mathbf{Q} \int\int_{-\infty}^{\infty} d^2\mathbf{S}\, U\left(\mathbf{S}+\frac{\mathbf{Q}}{2}\right) U^*\left(\mathbf{S}-\frac{\mathbf{Q}}{2}\right)$$

$$\times \exp\left[\frac{ik}{z}\left(\mathbf{S}-\mathbf{r}\right).\mathbf{Q}\right] \exp\left[-\frac{1}{2}D_{\mathrm{sp}}(Q)\right], \tag{2.2}$$

where $Q = |\mathbf{Q}|$ and $\mathbf{Q}$ is difference between two points in the wavefront, $\mathbf{S}$ is mean of two points in the wavefront and k is the angular wavenumber. We use the definition [(1), Eq. 6.70] for the structure function $D_{\mathrm{sp}}(Q)$, and, when $Q \ll l_0$, we find

$$D_{\mathrm{sp}}(Q) = 1.09C_n^2k^2z\, l_0^{-1/3}Q^2\left[1-0.72(k_0l_0)^{1/3}\right] \simeq 1.09C_n^2k^2zl_0^{-1/3}Q^2. \tag{2.3}$$

We note here that C_n is the refractive-index structure parameter, l_0 is the inner scale of the turbulence, and k_0 is the outer scale wavelength of the turbulence.

The particular aberration of interest is the quartic phase aberration that has been described by Siegman (11) and Siegman and Ruff (12),

$$U\left(r,\theta\right) = U_0\left(r,\theta\right)\exp\left[ik\left(\frac{r^2}{2F}-C_4r^4\right)\right]. \tag{2.4}$$

The quantity C_4 is the aberration strength of the non-ideal optical element, and F is the focal length. The initial beam is a Gaussian beam profile for which $U_0(\mathbf{r}, z = 0) = \exp\left(-r^2/W_0^2\right)$, where W_0 is the initial beam radius. The case in which the beam radius is a minimum at $z = 0$ will be presented here. In that case, we find

$$\frac{1}{2F} = \frac{2\overline{r^4}}{\overline{r^2}}. \tag{2.5}$$

Therefore, using Eqs. 2.4 and 2.5, the initial wave function of a Gaussian-distributed beam with quartic aberrations becomes

$$U(\mathbf{r}) = \exp\left[-\frac{r^2}{W_0^2} + ikC_4(2r^2W_0^2 - r^4)\right]. \tag{2.6}$$

Substituting Eq. 2.6 into Eq. 2.2 results in

$$\Gamma_2(\mathbf{r}, \mathbf{r}, z) = \left(\frac{k}{2\pi z}\right)^2 \int\int_{-\infty}^{\infty} d^2\mathbf{Q} \int\int_{-\infty}^{\infty} d^2\mathbf{S} \exp\left(\frac{2S^2}{W_0^2} - \frac{Q^2}{2W_0^2}\right)$$

$$\times \exp\left\{\frac{ik}{z}\left[1 + C_4 z\left(4W_0^4 - 4S^2 - Q^2\right)\right]\mathbf{S}\cdot\mathbf{Q} - \frac{ik}{z}\mathbf{r}\cdot\mathbf{Q}\right\} \exp\left[-\frac{1}{2}D_{\mathrm{sp}}(Q)\right]. \tag{2.7}$$

Even in the absence of turbulence, when $D_{\mathrm{sp}}(Q) = 0$, Eq. 2.7 cannot be analytically evaluated. However, the beam radius squared may be found using the moments method, starting from Eq. 2.1. To do so, we first let $G_0 \equiv \int\int_{-\infty}^{\infty} d^2\mathbf{r}\, \Gamma_2(\mathbf{r}, \mathbf{r}, z)$, so that

$$G_0 = \left(\frac{k}{2\pi z}\right)^2 \int\int_{-\infty}^{\infty} d^2\mathbf{Q} \int\int_{-\infty}^{\infty} d^2\mathbf{S} \exp\left(-\frac{2S^2}{W_0^2} - \frac{Q^2}{2W_0^2}\right)$$

$$\times \exp\left\{\frac{ik}{z}\left[1 + C_4 z\left(4W_0^4 - 4S^2 - Q^2\right)\right]\mathbf{S}\cdot\mathbf{Q}\right\}\delta\left(Q\right) = \left(\frac{k}{2\pi z}\right)^2 \frac{\pi}{2} W_0^2, \qquad (2.8)$$

where $\delta(\mathbf{Q})$ is the two-dimensional Dirac-delta function. We next calculate G_2, where $G_2 \equiv \int\int_{-\infty}^{\infty} d^2\mathbf{r}\, r^2\, \Gamma_2(\mathbf{r},\mathbf{r},z)$, so that

$$G_2 = \left(\frac{k}{2\pi z}\right)^2 \left(\frac{-z^2}{k^2}\right) \int\int_{-\infty}^{\infty} d^2\mathbf{S} \int\int_{-\infty}^{\infty} d^2\mathbf{Q}\delta\left(\mathbf{Q}\right) \nabla_{\mathbf{Q}}^2 \exp\left(-\frac{2S^2}{W_0^2} - \frac{Q^2}{2W_0^2}\right)$$

$$\times \exp\left\{\frac{ik}{z}\left[1 + C_4 z\left(4W_0^4 - 4S^2 - Q^2\right)\right]\mathbf{S}\cdot\mathbf{Q}\right\}$$

$$= \left(\frac{k}{2\pi z}\right)^2 \left[\pi\frac{W_0^4}{4} + \frac{\pi z^2}{k^2}\left(1 + 2k^2 C_4^2 W_0^8\right)\right]. \qquad (2.9)$$

We note here that $\nabla_{\mathbf{Q}}^2$ is the two dimensional Laplacian operator with respect to the coordinates $\left(Q_x, Q_y\right)$. Therefore, the beam radius squared in the absence of turbulence becomes

$$W^2(z) = 2\overline{r^2} = 2\frac{G_2}{G_0} = W_0^2 + \frac{4z^2}{k^2 W_0^2}\left(1 + 2k^2 C_4^2 W_0^8\right), \qquad (2.10)$$

so that the beam quality factor due to quartic aberrations is given by $M_{\mathrm{AB}}^2 = 2k^2 C_4^2 W_0^8$. This result is consistent with earlier calculations of Siegman (11) and Siegman and Ruff (12).

Adding the effect of turbulence is straightforward at this point. Since $\exp\left[-D_{\mathrm{sp}}(0)\right] = 1$, the quantity G_0 is unchanged. The ∇_{Q}^2 operation produces no interaction between turbulence terms and the other terms, so that

$$\nabla_{\mathrm{Q}}^2 \exp\left[-\frac{1}{2}D_{\mathrm{sp}}\left(Q\right)\right] = -\left(2.18C_n^2k^2zl_0^{-1/3} + \text{higher-order terms}\right)\exp\left[-\frac{1}{2}D_{\mathrm{sp}}\left(Q\right)\right]. \tag{2.11}$$

The higher-order terms in Eq. 2.11 are proportional to Q^2 and tend to zero as $Q \to 0$. Adding the turbulence contribution to the total beam radius squared, we obtain

$$\langle W^2(z)\rangle = 2\langle\overline{r^2}\rangle = 2\frac{G_2}{G_0} = W_0^2 + W_{\mathrm{diff}}^2 + \langle W_{\mathrm{turb}}^2\rangle + W_{\mathrm{AB}}^2, \tag{2.12}$$

where $W_{\mathrm{diff}}^2 = 4z^2/k^2W_0^2$, $\langle W_{\mathrm{turb}}^2\rangle = 2.18C_n^2l_0^{-1/3}z^3$ and $W_{\mathrm{AB}}^2 = 8z^2C_4^2W_0^6$. In the absence of aberrations, this equation is consistent with that in [(9), Eq. 18].

The turbulent contribution to M_{total}^4 for all distances is given by

$$M_{\mathrm{TU}}^2 = \frac{k^2W_0^2}{4z^2}\left(2.18C_n^2l_0^{-1/3}z^3\right) = 0.505C_n^2l_0^{-1/3}k^2zW_0^2, \tag{2.13}$$

so that in total

$$M_{\mathrm{total}}^4 = 1 + M_{\mathrm{AB}}^4 + M_{\mathrm{TU}}^4. \tag{2.14}$$

Using this expression, we plot M_{total}^2 vs. C_n^2 with $W_0 = 5$ cm and $l_0 = 4$ mm. Results are shown in Fig. 2.1, which should be compared to Fig. 6 in (14). While there are small differences due to our particular choices of the parameter values and different definitions of the M^2 factors, the behaviors are essentially the same, as we show in Fig. 2.1.

In order to verify this expression for an initial Gaussian beam, we calculated the beam radius squared $\langle W^2\rangle_{\mathrm{MC}} = 2\langle\overline{r^2}\rangle_{\mathrm{MC}}$, using the Monte Carlo technique, where $\langle\cdot\rangle_{\mathrm{MC}}$ denotes the ensemble average of the Monte Carlo realizations. We first write the paraxial

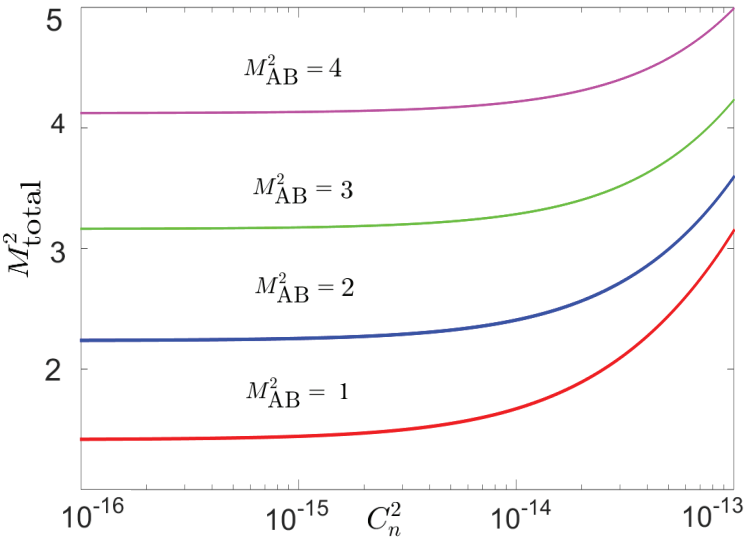

Figure 2.1: M^2_{total} vs. C_n^2

wave equation [(1), Eq. 7.3],

$$2ik\frac{\partial U(\mathbf{R})}{\partial z} + \nabla_T^2 U(\mathbf{R}) + 2k^2 n_1(\mathbf{R})\, U(\mathbf{R}) = 0, \tag{2.15}$$

where $\mathbf{R} = (\mathbf{r}, z)$ is the position vector, ∇_T^2 is the transverse Laplacian operator, $U(\mathbf{R})$ is the envelope of the electric field, and $n_1(\mathbf{R})$ is the randomly fluctuating portion of the atmosphere's refractive index. The solution of the wave equation, Eq. 2.15, over a small Δz can be written as

$$U(x, y, z + \Delta z) = U(x, y, z) \exp\left[ik \int_0^{\Delta z} dz' n_1(x, y, z')\right]. \tag{2.16}$$

We then write the first two statistical moments of $\theta \equiv k \int_0^{\Delta z} dz' n_1(x, y, z')$,

$$\langle \theta \rangle = k \int_0^{\Delta z} dz' \langle n_1(x, y, z') \rangle = 0 \tag{2.17}$$

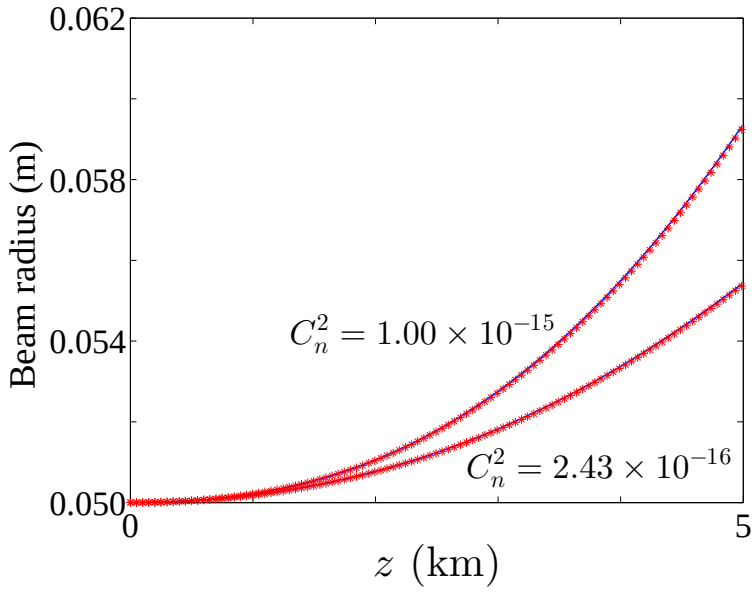

Figure 2.2: The solid lines ($-$) indicate the exact result, Eq. 2.12, and stars ($*$) indicate the Monte Carlo simulations

and

$$\langle [\theta]^2 \rangle = k^2 \int_0^{\Delta z} dz' \int_0^{\Delta z} dz'' \langle n_1(x,y,z') n_1(x,y,z'') \rangle. \tag{2.18}$$

We use the method of randomly varying phase screens, combined with the split-step method (13), to calculate $U(\mathbf{r},z)$ for a particular realization, and from that we calculate $\overline{r^2} = \int\int_{-\infty}^{\infty} d^2\mathbf{r}\, r^2 |U(\mathbf{r},z)|^2 / \int\int_{-\infty}^{\infty} d^2\mathbf{r}\, |U(\mathbf{r},z)|^2$. We use the von Karman-Tatarski (1) spectrum to calculate the phase screens. Averaging over 10^4 realizations, we obtain an estimate $\langle W^2(z) \rangle_{\mathrm{MC}} = 2\langle r^2(z) \rangle_{\mathrm{MC}}$. We show in Fig. 2.2 the comparison of Eq. 2.12 to Monte Carlo simulations with $W_0 = 5$ cm, $l_0 = 30$ mm, $C_4 = 0.08$ m^{-3}, and $\lambda = 1550$ nm. The agreement between the simulation and the exact solution is excellent as shown in Fig. 2.2.

We have also compared the Monte Carlo simulation results to field test data. In Fig. 2.3, we presents the spatial profiles of an infrared laser beam in a maritime environ-

ment at three different propagation distances. The data were captured off the Atlantic coast near Wallops Island, VA (15). These results can be compared to Fig. 2.4, which shows the IR spatial profiles of a Gaussian beam with over 10^4 iterations using Monte Carlo simulations at propagation distances of 5.1 km, 10.7 km, and 17.8 km. For the field experiment, a bi-directional infrared optical link was established between a lookout tower and a research vessel that was located in a range from about 5 km away from the lockout tower to almost the optical horizon distance of 17.8 km. The link was mechanically fixed and with adaptive optics pointing and tracking were maintained at the terminal. The data that are presented here were collected from the 2.54 cm diameter of optical lenes aperture, and the beam from the tower was transmitted from a 10-cm adaptive optics aperture. Observed realizations are each one-minute long. Samples of data were collected at a rate of 10^4 samples/second or 6×10^5 data points for the one-minute observation time, and then normalized to the mean of the data. We found that we had to use $C_n^2 = 1.2 \times 10^{-15}$ m$^{-2/3}$ at a propagation distances of 5.1 km and 17.8 km, and $C_n^2 = 4.0 \times 10^{-16}$ m$^{-2/3}$ at a propagation distance of 10.7 km to obtain good agreement between the probability distribution function (PDF) of our simulations and experiments . These values differ somewhat from the path average value of 2.4×10^{-15} m$^{-2/3}$ that was estimated at the time of the experiments, but are within the error range of this estimate. This estimate was rough, and, in fact, comparison to Monte Carlo simulations like ours (4) is an effective means of deducing the actual value. Additional details of the experimental set-up as well as the overall environmental characterizations can be found in (16) and (17).

Additionally, in Fig. 2.5, we show a comparison of the Monte Carlo simulations with the field test data at a propagation distance of 17.8 km with both the lognormal and gamma-gamma probability distribution function distributions (15). With moderate to strong turbulence fluctuations the gamma-gamma PDF should agree well with both our simulations and

(a) 5.1 km (b) 10.7 km (c) 17.8 km

Figure 2.3: IR spatial profiles of the propagating beam from data collected near Wallops Island, VA (16).

experiments. The fluctuation regime is characterized by the Rytov variance (1),

$$\sigma_R^2 = 1.23 C_n^2 k^{7/6} z^{11/6}. \tag{2.19}$$

The weak fluctuation regime corresponds to $\sigma_R^2 < 1$, while the moderate-to-strong fluctuation regime corresponds to $\sigma_R^2 > 1$. For our simulations, the Rytov variance is 4.7, and, for the experiments, it is 10.5 at 17.8 km; so, the system is in the moderate to strong fluctuation regime. Our results are consistent with those in (18).

Table 1 shows a comparison of the scintillation index that we obtain from our Monte Carlo simulations and from our experiments. The scintillation index is a measure of the degree of fluctuation that a signal's amplitude experiences due to passage through turbulence. The scintillation index is defined as the irradiance variance scaled by the square of the mean irradiance (1),

$$\sigma_I^2(\mathbf{r}, z) = \frac{\langle I^2(\mathbf{r}, z) \rangle}{\langle I(\mathbf{r}, z) \rangle^2} - 1, \tag{2.20}$$

where the irradiance is equal to mutual coherence function, $\langle I(\mathbf{r}, z) \rangle = \Gamma_2(\mathbf{r}, \mathbf{r}, z)$, and the second moment of the irradiance is the fourth-order coherence function, $\langle I^2(\mathbf{r}, z) \rangle = \Gamma_4(\mathbf{r}, \mathbf{r}, \mathbf{r}, \mathbf{r}, z)$. In order to calculate the scintillation index of the simulation, we used 10^4 realizations, and we used the peak intensity for each run to calculate the irradiance vari-

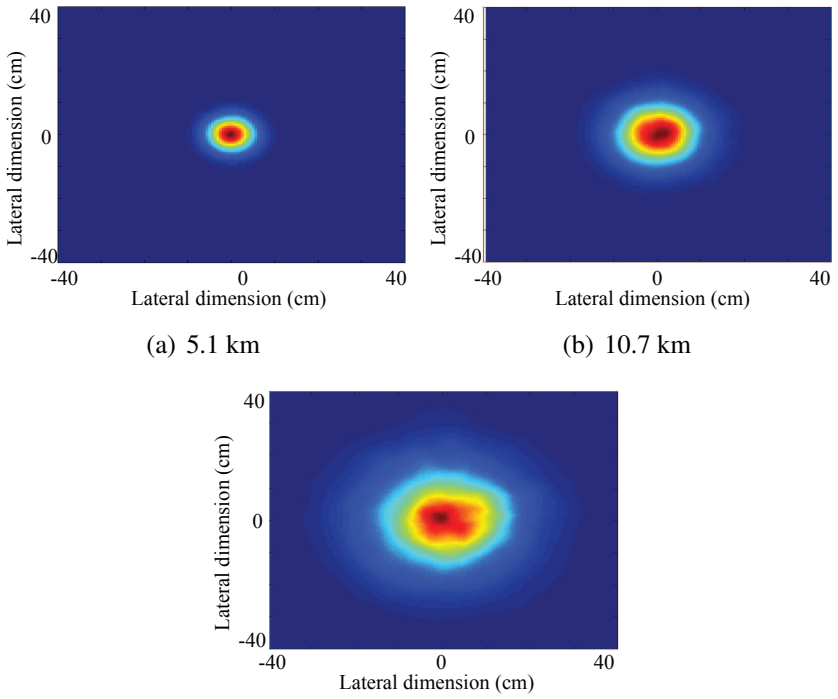

(a) 5.1 km (b) 10.7 km

(c) 17.8 km

Figure 2.4: IR spatial profiles of a Gaussian beam using Monte Carlo simulations averaged over 10^4 realizations at three different propagation distances.

ance and square of mean irradiance. In the experiments, the scintillation index is computed directly from the data run. As can be seen in Table 1, the scintillation increases as the distance increases. The agreement between the scintillation index of the simulations and experimental results is very good at all distances as shown in Table 1. As was mentioned previously, we found that we had to use $C_n^2 = 1.2 \times 10^{-15}$ m$^{-2/3}$ at a propagation distances of 5.1 km and 17.8 km, and $C_n^2 = 7.0 \times 10^{-16}$ m$^{-2/3}$ at a propagation distance of 10.7 km to obtain good agreement for scintillation index and PDF between our simulations and experiments. The results indicate the utility of using Monte Carlo simulations to obtain good estimates of the turbulence parameters.

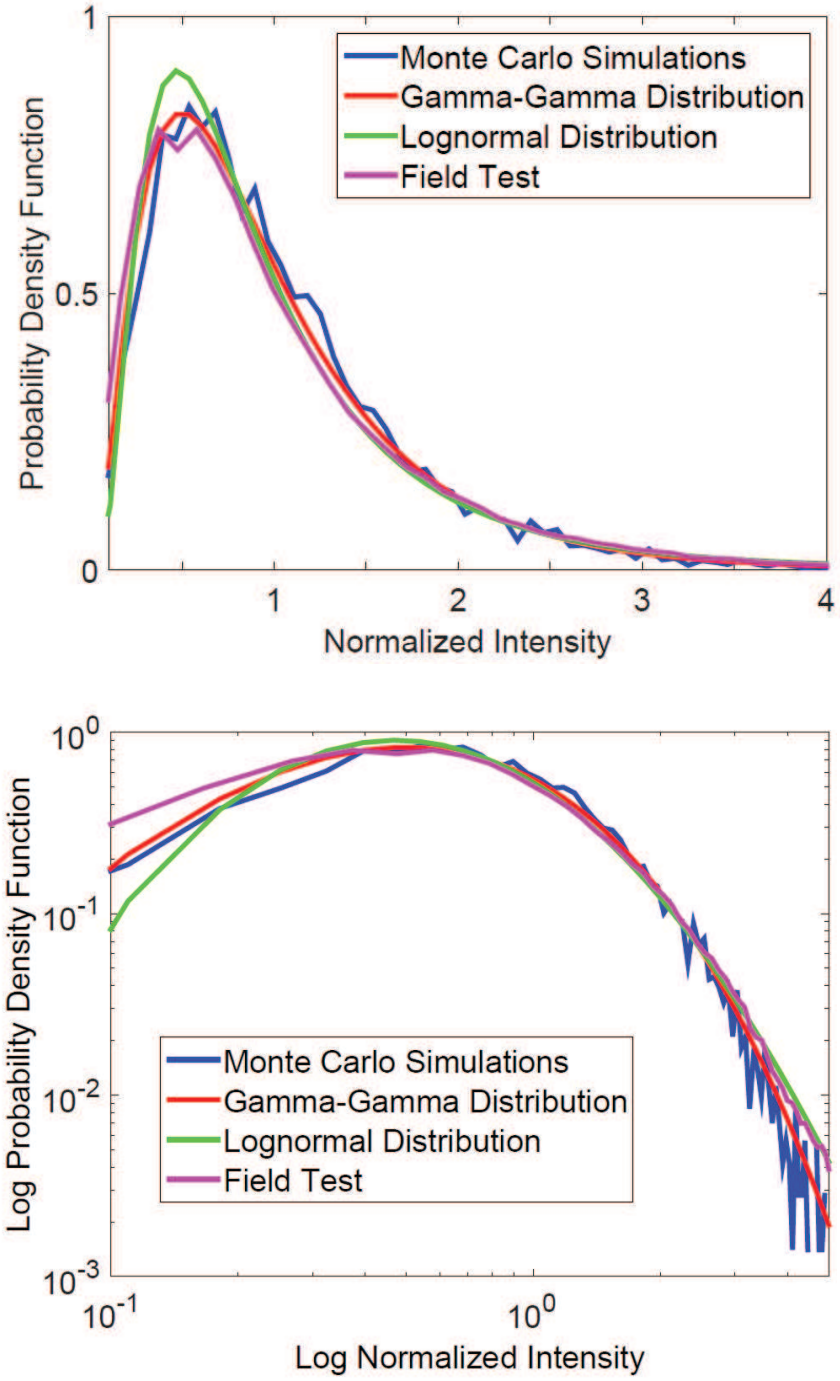

Figure 2.5: Comparison of the Monte Carlo simulations and the field test at a propagation distance of 17 km with the lognormal and gamma-gamma PDF models. (a) The probability density function of the normalized intensity. (b) Probability density function of the normalized intensity shown on a log-log plot.

	Scintillation Index	
Distance	Simulations	Experiment
5.1 km	0.066	0.066
10.7 km	0.127	0.123
17.8 km	0.662	0.635

Table 2.1: Simulation vs. field test data

2.2 Beam spreading in the presence of atmospheric turbulence

In this project, we showed that the turbulence contribution $\langle W_{\text{turb}}^2 \rangle$ to the beam radius squared, is proportional to distance z^3 for all distances and for all refractive-index structure parameters C_n^2, in contrast to a classical result due to Fante (2). We have shown in Eq. 2.12 that $\langle W_{\text{turb}}^2 \rangle = 2.18 C_n^2 l_0^{-1/3} z^3$. This formula is in agreement with Fante [(2), Eq. 37a] at long distances, but is in disagreement with Fante [(2), Eq. 37] and the result that was reproduced by Andrews and Phillips (1) at short distances. This discrepancy is due to an approximation of the structure function, which becomes invalid at small Q. We may write the spherical wave structure function as [(1), 6.67]

$$D_{\text{sp}}(Q) = 8\pi^2 k^2 z \int_0^1 \int_{-\infty}^{\infty} \kappa \Phi_n(\kappa) \left[1 - J_0(\kappa \xi Q)\right] d\kappa d\xi. \tag{2.21}$$

A useful form for $D_{\text{sp}}(Q)$ may be obtained by explicitly expanding the Bessel function to yield

$$D_{\text{sp}}(Q) = 8\pi^2 (0.033) C_n^2 k^2 z \sum_{n=1}^{\infty} \frac{(-1)^{n-1} Q^{2n}}{2^{2n}(2n+1)(n!)^2} \times \int_0^{\infty} \kappa^{2n+1} \Phi_n(\kappa)\, d\kappa. \tag{2.22}$$

In the limit $Q \to 0$, we find $D_{\text{sp}}(Q) = 0.022\pi^2 C_n^2 k^2 z Q^2 A$, where $A = \int_0^{\infty} \kappa^3 \Phi_n(\kappa)\, d\kappa$ is independent of both Q and z. The salient points to note are: (1) This Taylor expansion

of $D_{\rm sp}(Q)$ in powers of Q^2 is absolutely convergent and has Q^2 as its lowest-order power; (2) $D_{\rm sp}(Q)$ is strictly proportional to z. These points hold for any $\Phi_n(\kappa)$, so that the scaling that we derive for $\langle\overline{r^2}\rangle$ as a function of z holds for any $\Phi_n(\kappa)$. An expression that closely approximates Eq. 2.21 [(1), 6.70] for $Q \ll l_0$ is

$$D_{\rm sp}(Q) \simeq 1.09 C_n^2 k^2 z l_0^{-1/3} Q^2, \tag{2.23}$$

and for $Q \gg l_0$ is

$$D_{\rm sp}\,(Q) \simeq 1.09 C_n^2 k^2 z Q^{5/3}. \tag{2.24}$$

Fante (2) used Eq. 2.23 at long distances and Eq. 2.24 at short distances, which allowed him to calculate an explicit approximation for $\Gamma_2(\mathbf{r},\mathbf{r},z)$ using Eq. 2.2, which he then substituted into Eq. 2.1 to calculate the beam radius. As we have shown, the mean square beam radius $\langle r^2\rangle$ is entirely determined by the behavior at $Q = 0$, where the approximation for $D_{\rm sp}$ breaks down and $D_{\rm sp}\,(Q) \propto Q^2$. We show the difference between Fante's approximation for $D_{\rm sp}\,(Q)$ and the exact expression for $D_{\rm sp}\,(Q)$ in Fig. 2.6. In order to verify this expression for an initial Gaussian beam, we used Monte Carlo simulations. Averaging over 10^4 realizations, we obtain an estimate $\langle W^2\,(z)\rangle_{\rm MC} = 2\langle r^2\,(z)\rangle_{\rm MC}$. In Fig. 2.7, we show a comparison of the Monte Carlo simulations at short distances to both the exact result, Eq. 2.12, in the absence of abberations, and Fante's expression [(2), Eq. 37]. We show the turbulence contribution $\langle W^2_{\rm turb}\rangle_{\rm MC} = \langle W^2\rangle_{\rm MC} - W_0^2 - W^2_{\rm diff}$. The Monte Carlo simulations agree well with the exact result. Using a least-square fit to the variation of $\log\langle W^2_{\rm turb})\rangle_{\rm MC}$ with distance, we find that the 95% confidence interval for the slope is 3.0146 ± 0.0235, which is in agreement with the exact formula. the deviation grows on a logarithmic scale as Q becomes small. This deviation at small Q translates into a difference in the beam intensity at large r. As shown in Fig. 2.8, the intensity using Fante's expression has a tail at large r in contrast to the intensity using the exact expression, which

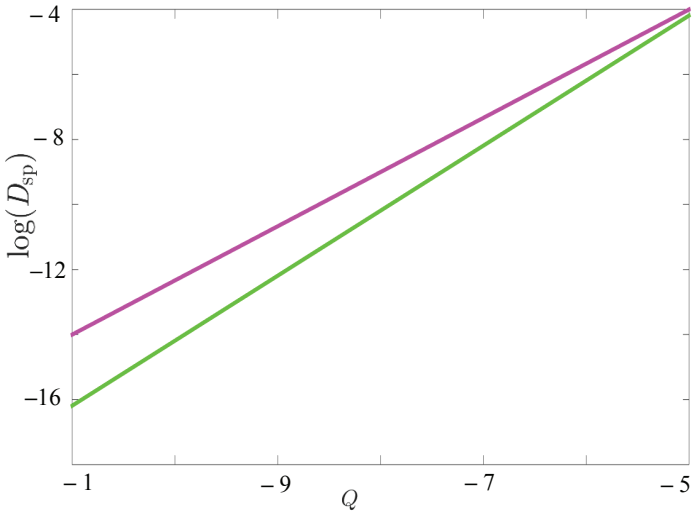

Figure 2.6: D_{sp} vs. Q for short distances. We compare the exact and approximate expressions. The red line indicates $D_{\text{sp}}(Q) = 1.09 C_n^2 k^2 z Q^{5/3}$. The green line indicates $D_{\text{sp}}(Q) = 1.09 C_n^2 k^2 z l_0^{-1/3} Q^2$

is Gaussian-distributed at all distances.

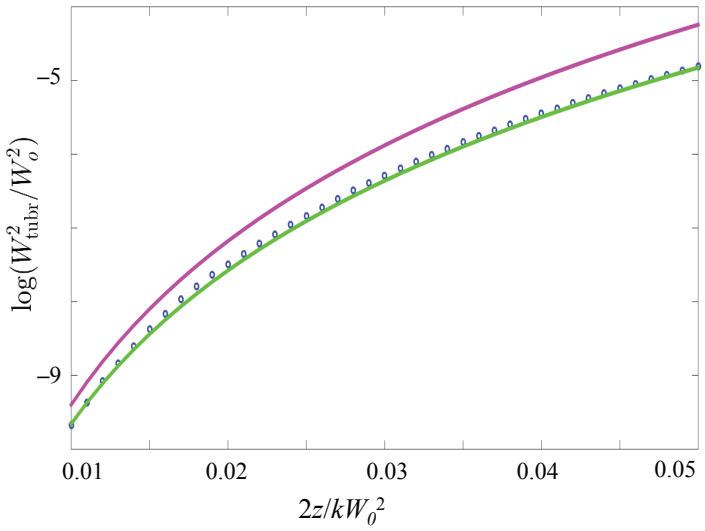

Figure 2.7: Turbulence contribution to the beam radius squared for short distances, where $\lambda = 630$ nm, $l_0 = 0.011$ m, $C_n = 7.0 \times 10^{-15}$ m$^{-2/3}$. The green line indicates the exact result, the red line indicates Fante's result, and open circles (○) indicate the Monte Carlo result.

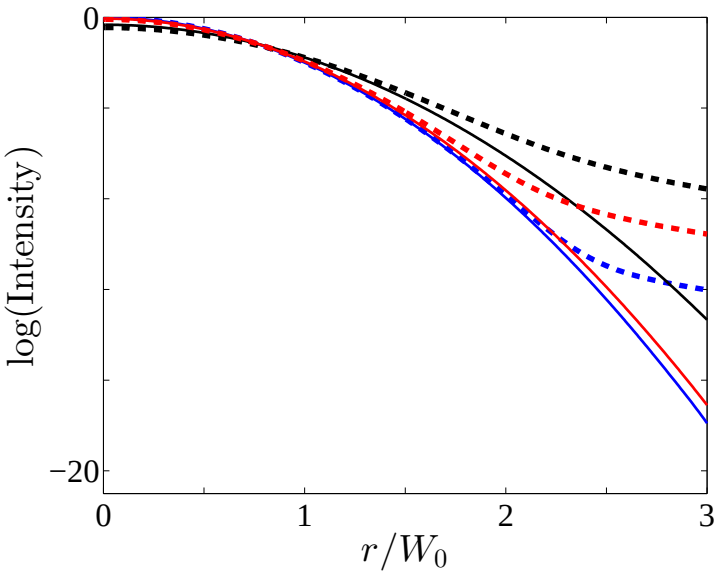

Figure 2.8: Intensity as a function of radius, normalized to the initial peak intensity. Using Fante's expression for D_{sp} at short distance leads to incorrect results at large r. Dashed lines indicates intensities with $D_{\text{sp}}(Q) = 1.09C_n^2k^2zQ^{5/3}$. Solid lines indicates intensities with $D_{\text{sp}}(Q) = 1.09C_n^2k^2zl_0^{-1/3}Q^2$. Blue, red, and black indicate respectively $\bar{z} = 2z/kW_0^2 = 0.01, 0.03, 0.06$.

Chapter 3

Partially coherent beam propagation through turbulence

3.1 Simulations description

We investigated the possibility of decreasing the receiver scintillations by reducing the spatial coherence of the beam and thereby improving the bit error ratio. A laser beam propagating in free space can undergo significant random intensity fluctuations due to turbulence along the propagation path. A coherent beam (CB) becomes partially coherent when it propagates in atmospheric turbulence, especially in strong turbulence. The theory developed by Banach et al. (19) and by Ricklin and Davidson (20) that models a spatially partially coherent source beam, as applied to atmospheric turbulence for the communication channel, shows that it is possible to decrease the receiver scintillations in some cases by reducing the spatial coherence of the beam and thereby improving the bit error ratio (BER).

We focused on the simulation of a partially spatially coherent laser beam and compared the results with the field test data for both terrestrial and maritime environments. Experimental and simulation implementation of the partially coherent laser light has been accomplished using a spatial light modulator (SLM) for both visible (HeNe) and infra-red

(IR) frequencies. A spatial light modulator allows direct control over the phase front of the laser beam. We can generate a partially spatially coherent beam by passing a coherent Gaussian beam through a random phase screen. Most studies consider the Gaussian Schell-model (GSM) beam, which is an analytically tractable model in which the beam field amplitude distribution and the spatial coherence function are both Gaussian. We developed a MATLAB code to generate a random phase screen using a technique described by Shirai, Korotkova, and Wolf (21). The initial GSM beam can be written as

$$V_0(\mathbf{r}) = V(\mathbf{r}, z = 0) = \exp\left(-\frac{r^2}{W_0^2}\right) \exp\left[i g_\phi(r)\right], \tag{3.1}$$

where $\mathbf{r} = (x, y)$ is the transverse vector, $r = |\mathbf{r}|$ is the magnitude of the transverse vector, z is the propagation distance, W_0 is the initial beam radius, and $g_\phi(r)$ is a Gaussian-correlated random function and can be written as a convolution integral,

$$g_\phi(r) = \int f_\phi(r - r') R_\phi(r') d^2 r'. \tag{3.2}$$

The quantity $R_\phi(r)$ is a two-dimensional real-valued random function that is Gaussian-distributed with zero mean, while $f_\phi(r)$ is a window function and is given by

$$f_\phi(r) = \exp\left(-\frac{r^2}{\gamma_\phi^2}\right), \tag{3.3}$$

where γ_ϕ is a positive constant. Figure 3.1 shows sample phase screens with different values of γ_ϕ^2 that were used in our simulations and experiments.

In order to model the propagation of a GSM beam through turbulence, we use the same method that was described in chapter 2.1.

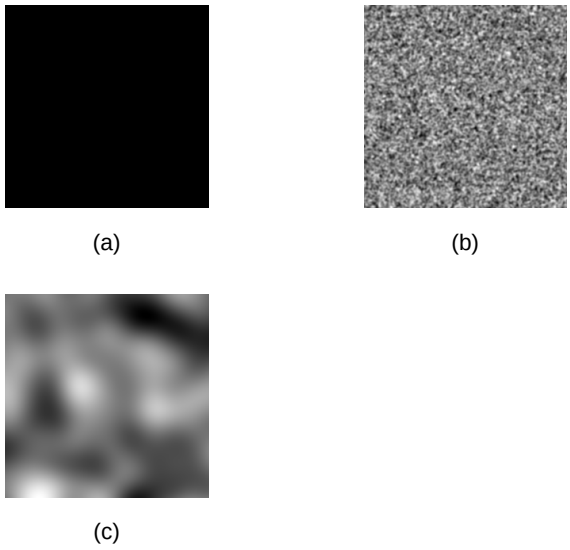

Figure 3.1: (a) $\gamma_\phi^2 = \infty$ (coherent), (b) $\gamma_\phi^2 = 1$ (strong diffuser), (c) $\gamma_\phi^2 = 16$.

3.2 Field TEST Description

For the USNA field test, both an IR (1550 nm) and a HeNe (632.8 nm) laser were used. The IR laser beam was used over land with a 180-m propagation distance, and the HeNe laser was used over water with a 314-m propagation distance as shown in Fig. 3.2. In both experiments, the laser beam was vertically polarized, went through a beam expander (IR and visible), was reflected from a 7.68 mm $\times$ 7.68 mm SLM (IR and visible), and then propagated through the atmosphere to a target receiver. At the receiver, an amplified photodetector and data acquisition system were used to collect data at 10,000 samples/second. Each data run was approximately two minutes in duration. A scintillometer was used to estimate the value of refractive-index structure parameter, C_n^2, over the propagation path for both field tests. We measured $C_n^2 = 1 \times 10^{-14}$ m$^{-2/3}$ for the 314-m path over a creek. We suspect that the scintillometer was misaligned during the 180 m terrestrial test, and we therefore estimated $C_n^2 = 1 \times 10^{-15}$ m$^{-2/3}$ based on previous measurements. For more details on the field test data, see (22).

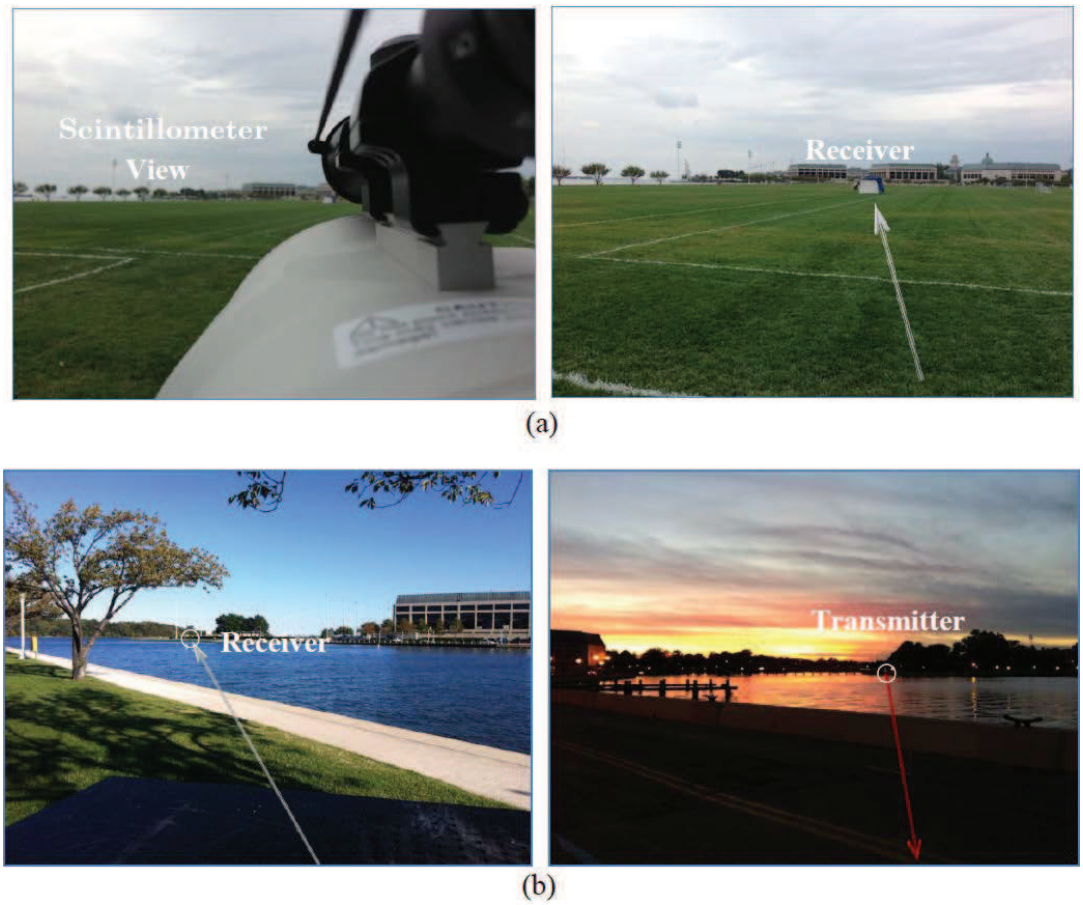

Figure 3.2: USNA field tests, arrows show direction of laser beam propagation (a) 180 m IR (1550 nm) laser beam propagation, scintillometer view is seen in left hand image, (b) 314 m HeNe (632.8 nm) laser beam propagation over creek. Left-hand side is the transmitter view, and the right-hand side image is the receiver side view. Scintillometer was aligned along beam path (22).

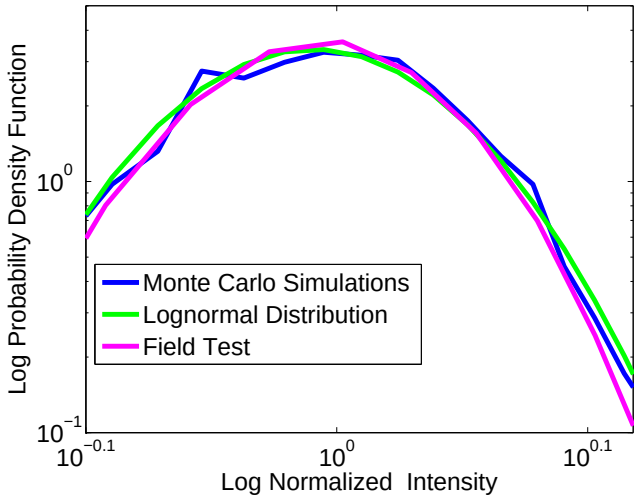

Figure 3.3: Comparison of the Monte Carlo simulations and the field test with a degree of coherence $\gamma_\phi^2 = 2$ to the lognormal PDF model for the IR beam at a propagation distance of 180 m.

3.3 Field test data vs. Simulations

Figures 3.3 and 3.4 show a comparison of the Monte Carlo simulations, the field test data at a propagation distance of 314 m for the HeNe laser and 180 m for the IR beam, and lognormal PDF distributions. In order to match the probability distribution function from the simulations to the field test data, we used $C_n^2 = 1 \times 10^{-13}$ $\mathrm{m}^{-2/3}$ for the IR beam, and we used $C_n^2 = 8 \times 10^{-15}$ $\mathrm{m}^{-2/3}$ for the HeNe beam. These values differ somewhat from the path average values that were estimated at the time of the experiments, but are within the error ranges of these estimates. These estimates were rough, and, in fact, comparison to Monte Carlo simulations like ours is an effective means of deducing the actual values. With weak turbulence fluctuations, the lognormal PDF should agree well with both our simulations and experiments. For the HeNe beam propagation, the Rytov variance is $\sigma_R^2 = 0.05$ and for the IR beam propagation, it is $\sigma_R^2 = 0.08$; so, these experiments are in the weak fluctuation regime.

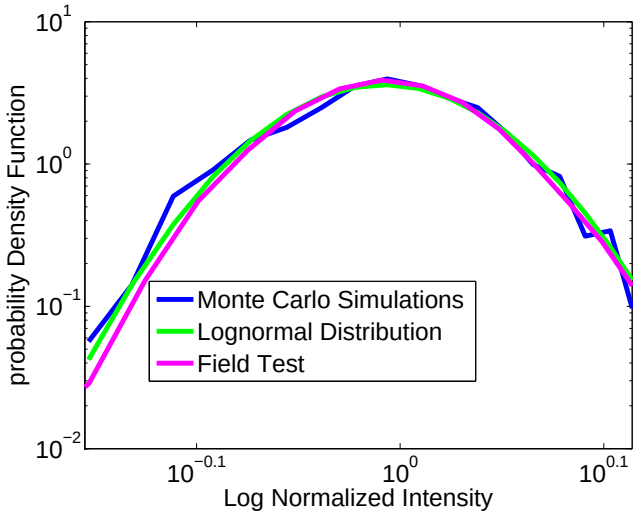

Figure 3.4: Comparison of the Monte Carlo simulations and the field test with a degree of coherence $\gamma_\phi^2 = 2$ to the lognormal PDF model for the HeNe beam at a propagation distance of 314 m.

Tables 3.1 and 3.2 show a comparison of the scintillation index for varying spatial coherence from fully coherent to nearly incoherent that we obtained from Monte Carlo simulations and from the experiments for the IR beam over 180 m and the HeNe beam over 314 m.

For the IR beam simulations, the strongest diffusers, which correspond to $\gamma_\phi^2 = 1$ through 8, have higher scintillation indices than the fully coherent beam. The scintillation index is lower than the coherent beam for the partially spatially coherent beam with $\gamma_\phi^2 = 16$ and $\gamma_\phi^2 = 128$, which constitute "possible sweet spots" of the scintillation indices. Values of γ_ϕ^2 at which the scintillation index is less than its value for the coherent beam have been referred to as "possible sweet spots" (22). By "possible" we mean that the value of γ_ϕ^2 at which a "sweet spot" occurs depends on C_n^2 and z. For the IR beam experiment, we find a possible sweet spot at $\gamma_\phi^2 = 32$. Table 3 shows the scintillation results for the HeNe beam. The simulation results indicate that γ_ϕ^2 = 16 is a possible sweet spot. The HeNe experimental results indicate that all values of γ_ϕ^2 in the range of $1 \leq \gamma_\phi^2 \leq 64$ are possible

	Scintillation	
γ_ϕ^2	Simulations	Experiment
Black (coherent)	0.0114	0.0063
1 (Strong diffuser)	0.0132	0.0110
2	0.0170	0.0121
4	0.0136	0.0105
8	0.0120	0.0102
16	*0.0110*	0.0079
32	0.0114	*0.0057*
64	0.0115	0.0077
128 (weak diffuser)	*0.0113*	0.0074

Table 3.1: Scintillation Indices for the IR laser beam at a propagation distance of 180 m with a varying spatial coherence for both field test data [18] and simulations. The italicized numbers indicate possible scintillation index sweet spots.

sweet spots. The simulations are in the reasonable agreement with the experiments, given experimental uncertainties in C_n^2. Both simulation and experiment indicate that possible sweet spots exist for both the IR and HeNe laser beams. We attribute the differences in the scintillation indices between the field test data and the simulations primarily to errors in the estimates of the C_n^2 in the experiment, but we also note that the photodetector had a lense aperture of 2.45 cm at the test setup, while the simulation used point measurements of the center intensity profile in order to save computation time.

In Figs. 3.5(a) and (b), we show the beam spreading for the HeNe beam, both with and without turbulence, for the coherent beam and partially coherent beam in the case $\gamma_\phi^2 = 16$. As expected, the partially coherent beam spreads more both with and without turbulence than does the coherent beam. In order to investigate the effect of beam spreading that is due only to turbulence, we look at the relative beam spread, which is the difference between the beam spread without turbulence and with turbulence for each case. The relative

	Scintillation	
γ_ϕ^2	Simulations	Experiment
Black (coherent)	0.0076	0.0119
1 (Strong diffuser)	0.0090	*0.0101*
2	0.0124	*0.0115*
4	0.0093	*0.0107*
8	0.0080	*0.0095*
16	*0.0073*	*0.0107*
32	0.0076	*0.0094*
64	0.0076	*0.0095*
128 (weak diffuser)	0.0075	0.0122

Table 3.2: Scintillation indices for the HeNe laser beam at a propagation distance of 314 m with varying spatial coherence for both field test data [18] and simulations. The italicized numbers indicate possible scintillation index "sweet spots", where the scintillation index of partially coherent beam is less than coherent beam.

beam spread for both the HeNe beam and the IR beam is presented in Figs. 3.6(a) and (b). The results show that relative beam spread is lower for partially coherent beams than it is for coherent beams. We conclude that partially coherent beams are less distorted by atmospheric turbulence than are coherent beams in cases where the scintillation indices of the partially coherent beams are smaller than is the scintillation index of a coherent beam.

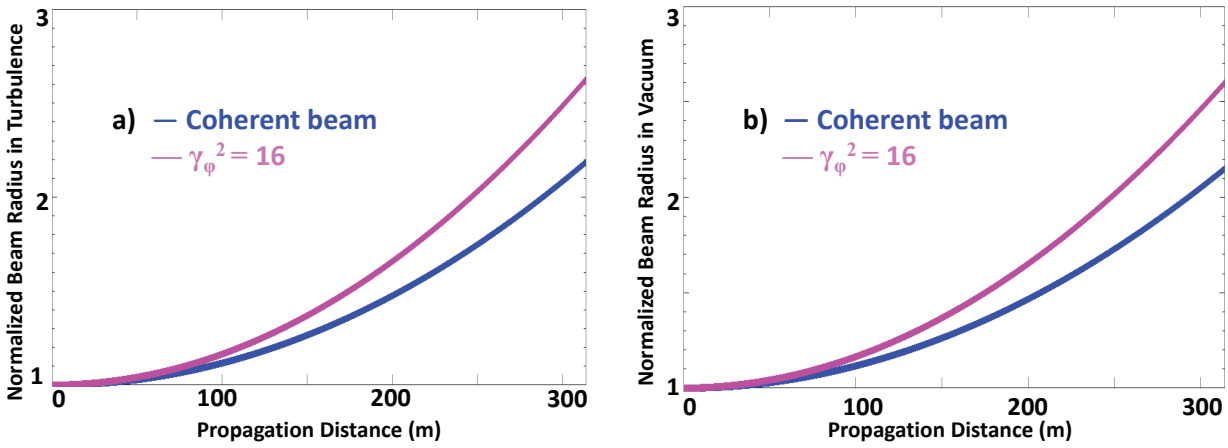

Figure 3.5: The beam spreading for the HeNe beam for a coherent and a partially coherent beam with $\gamma_\phi^2 = 16$ at a propagation distance of 314 m (a) with turbulence and (b) without turbulence.

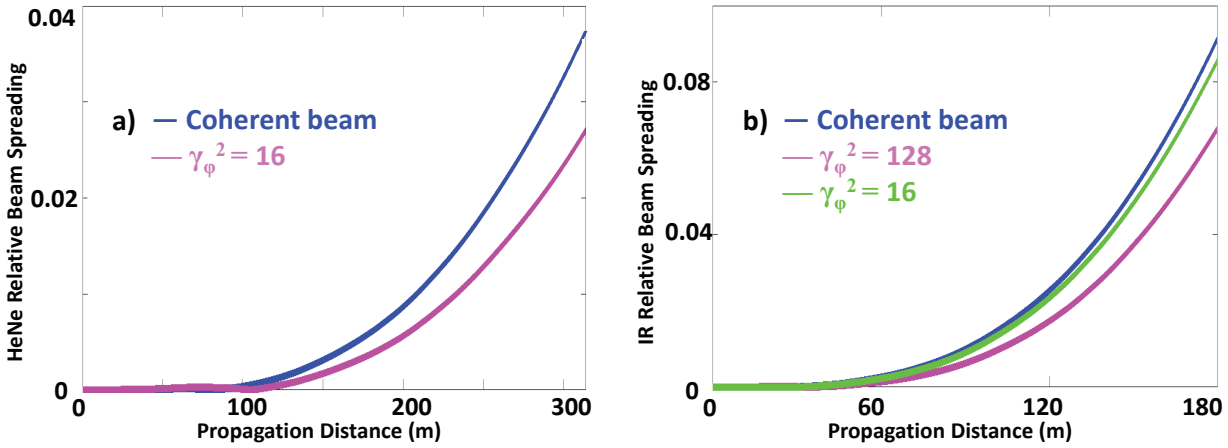

Figure 3.6: Relative beam spreading for a coherent and a partially coherent beams: (a) HeNe beam at a propagation distance of 314 m and (b) IR beam at a propagation distance of 180 m.

Chapter 4

Solar scintillation study during planetary conjunction: Data analysis

4.1 RF beam propagation through Solar Corona

The goal of this project is to investigate the effect of an RF X-band signal as it propagates through the solar corona in superior solar conjunction at low Sun-Earth-Probe (SEP) angles. This information is needed for existing and planned missions in which spacecraft operate near conjunction, such as STEREO, and solar Probe Plus. A superior conjunction occurs when a solar system body or a spacecraft lies along a straight line joining the Earth and the Sun, but is on the opposite side of the Sun from the Earth, as shown in Fig. 4.1. During superior conjunction the spacecraft has limited communication with the ground station due to the effects of the Sun on the RF signal transmission. In order to analyze RF beam propagation at superior solar conjunction with a low SEP angle, we analyzed the recent data obtained during superior solar conjunction of the MESSENGER (MErcury Surface, Space ENivornment, GEochmeisty, and Ranging) spacecraft at X-band for days 114, 115, 339, 340, and 344 for year 2014, for a Sun-Earth-Probe (SEP) angle between 0.7° to 1.84°. MESSENGER was the Johns Hopkins University Applied Physics Laboratory mission to Mercury. It was launched in 2004, and it was in orbit around Mercury from March 18, 2011

Date	DSS Location	Start Time	End Time	Start SEP angle	End SEP angle
DOY 114 2014	25 Goldstone	57902 s	86400 s	1.7961°	1.4344°
DOY 115 2014	65 Madrid	23402 s	60600 s	1.1443°	0.7017°
DOY 339 2014	35 Canberra	76625 s	86400 s	1.6114°	1.5622°
DOY 340 2014	55 Madrid	33611 s	52200 s	1.14037°	1.3305°
DOY 344 2014	15 Goldstone	59666 s	70133 s	1.7946°	1.8497°

Table 4.1: Data analysis information

until April 30, 2015.

In this chapter we will focus on the data analysis and next chapter on the theocratical model.

4.2 Observation

The Deep Space Network (DSN) Radio Science Receiver (RSR) records a carrier signal from the spacecraft, and the subcarriers are filtered. The DSN RSR captured the MESSENGER's X-band downlink throughout the Deep Space Station (DSS). For Day of Year (DOY) 114, 115, 339, and 340, the spacecraft entered superior solar conjunction, so that as the time increased the angle decreased. During DOY 344 the spacecraft egressed from superior solar conjunction. Information on DOY, DSS location along with the dish number, time and SEP angle is shown in Table. 4.1.

The data from MESSENGER for both DOY 114 and 115 were initially transmitted through the low gain antenna (LGA) and later through the high gain antenna (HGA) for the rest of the contact. During DOY 340, data were transmitted exclusively through LGA and for DOY 339 and DOY 344 exclusively through HGA.

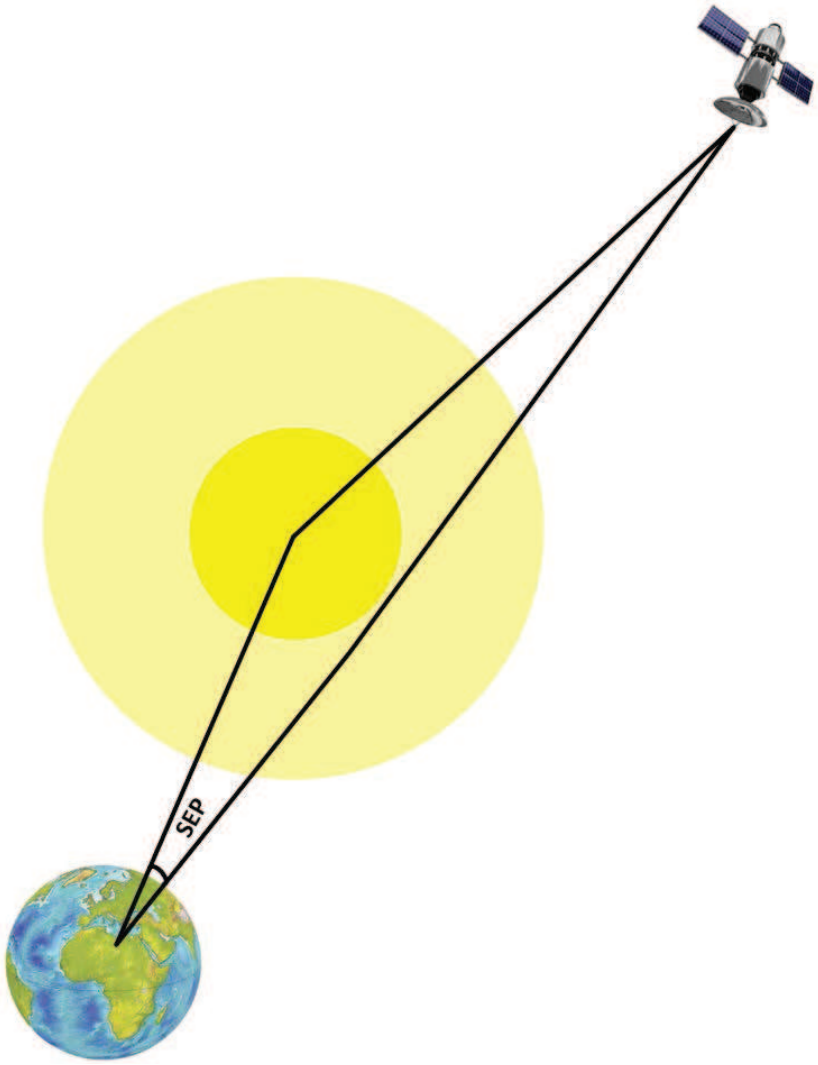

Figure 4.1: Spacecraft in superior solar conjunction. The distance that the signal propagates through the corona and solar wind is a function of the SEP angle. For this data set, the distance was approximately 274 solar radii, the straight line from spacecraft to earth.

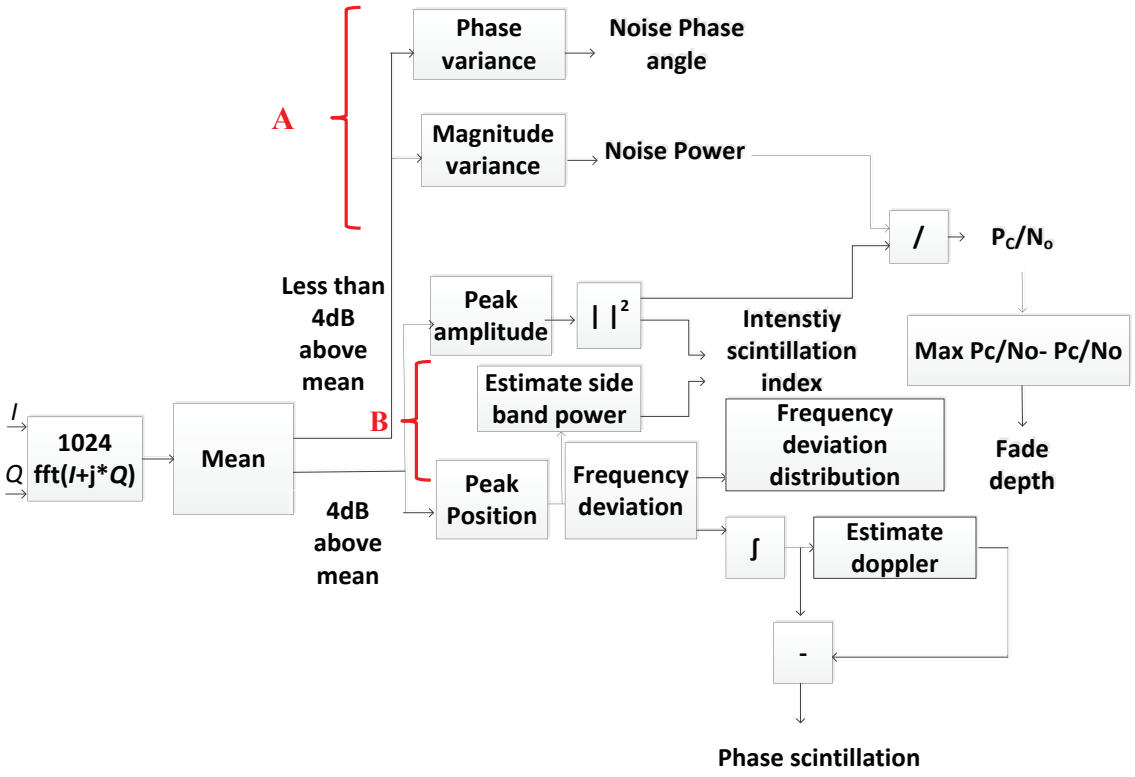

Figure 4.2: Data analysis process

4.3 Analysis Process

The data sample rate at the RSR was 1 ksps in the form of in-phase (I) and quadrature-phase (Q) samples. We transformed the time-sampled I/Q data to the frequency domain, using a 1024-point FFT (duration approximately one second), so that each bin has a resolution of approximately 1 Hz. Also the auxiliary SEP angle data provided to us was available in one-second intervals. In Fig. 4.2, we show a flow chart for the entire data analysis.

4.4 Estimation of Noise Power and Peak Amplitude

The noise power is obtained by calculating the variance of the amplitude fluctuations after excluding amplitudes that are 4 dB above the average, as shown in Fig. 4.2, marked as **A**. We chose a 4-dB threshold to prevent strong signals from biasing our estimate. We found that the noise power is independent of the SEP angle and that there is no correlation between the SEP angle and the noise power. We further found that the phase variance of the same bins were independent of SEP angle. Therefore, we conclude that phase scintillation is obscured by antenna thermal noise on a one-second time scale.

We next proceeded to investigate the peak amplitude (carrier) and peak amplitude position for a 1024-point FFT as illustrated in Fig. 4.2, marked as **B**. These data were recorded for each bin. The peak power is obtained by squaring the peak amplitude in each bin. The peak power for day 115 where the SEP angle is the smallest, between 0.7° to 0.9°, shows that there is a slight power loss with decreasing SEP due to scattering of the signal away from the line-of-sight, as shown in Fig. 4.3. We describe the variation of the peak amplitude position in the next section.

4.5 Frequency Deviation

The peak amplitude position for each 1024-point FFT is recorded, as illustrated in Fig. 4.2, marked as **A**. The peak amplitude position for DOY 114, 339, 340, and 344, shows a systematic frequency deviation due to a spacecraft Doppler shift in approximately four-hour periods. That is visible in Figs. 4.4(b), (c), (d), and (e). During these days, the SEP angle changes from 1.33° to 1.84°. On DOY 115, there is a systematic frequency deviation in the four-hour periods due to both the spacecraft's Doppler shift and broadening due to solar scintillation, as shown in Fig. 4.4(a). We stress that the time scale of the changes in frequency due to the Doppler shift or due to frequency modulation from solar scintillation

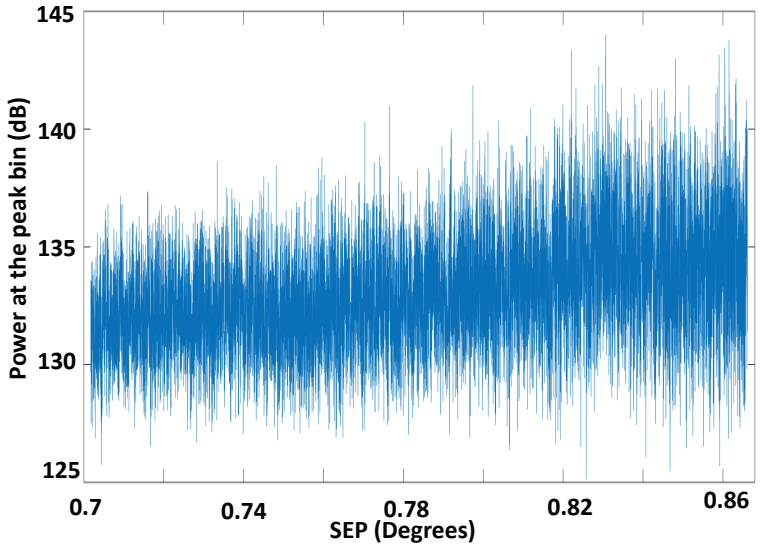

Figure 4.3: Peak power for an SEP angle between 0.7° to 0.86°

is on order of hours. Therefore on the time scale of data frames, there will be no measurable frequency modulation and no spectral broadening for SEP $> 1.0°$.

We have also investigated the bin shift distributions of the peak amplitude. In order to find the frequency deviation distribution, we estimate the running average over 100 seconds of all the peak positions, and we find the shifts for each bin from the running mean. In Fig. 4.5, we plot the frequency distribution for every 1000 points. The SEP angle is approximately constant over this time interval. Examination of the distribution of the peak positions shows that the frequency deviation increases as the SEP angle decreases, and the variance for an SEP angle of 0.7° is larger than for an SEP angle of 0.8°, as shown in Fig. 4.5.

4.6 Phase Scintillation

Phase scintillation arises from frequency fluctuations that are imposed on the carrier by fluctuations in the solar plasma. In order to calculate the phase scintillation, we per-

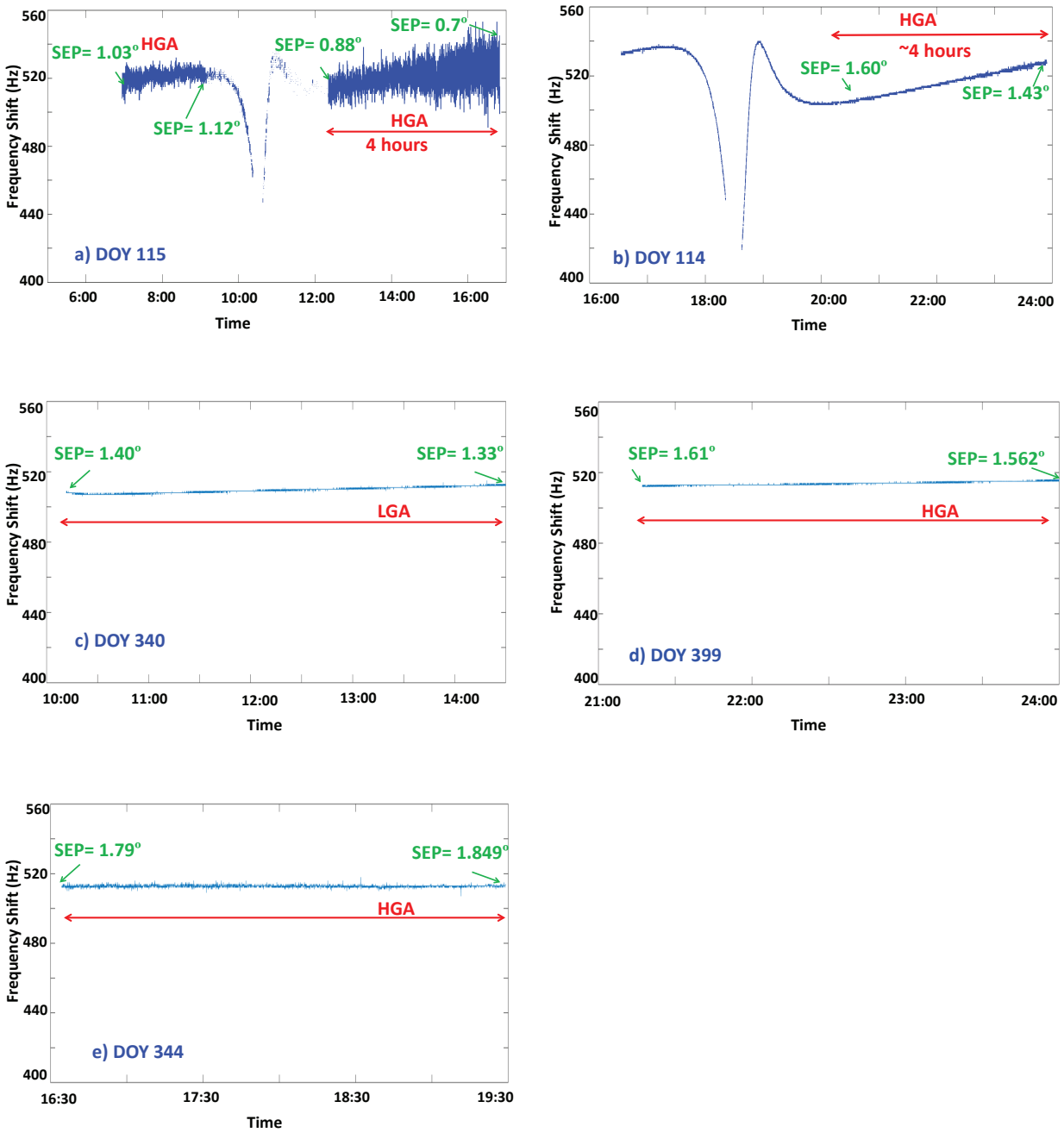

Figure 4.4: Frequency deviation for DOY 114, DOY 115, DOY 339, DOY 340, and DOY 344.

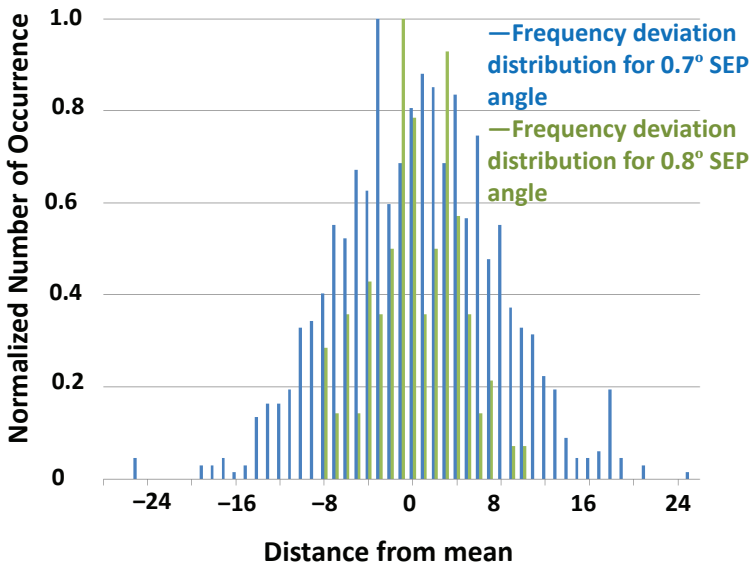

Figure 4.5: Frequency deviation distribution for SEP angles of 0.7° and 0.8°.

formed a 1024-point FFT about some instant k, and we found the frequency bin n in which the peak occurred. We denote this frequency bin by $f_n(k)$. Next, we repeated the same process at the next instant, $k+1$, and we determined the frequency bin m at which the peak occurred. The difference between two consecutive bins, $[f_m(k+1) - f_n(k)]\Delta t = \Delta f(k)\Delta t$, where $k = 1, 2, ...,$ and Δt is approximately 1 second, as shown in Fig. 4.6.

The instantaneous phase is by definition (25)

$$\Phi = 2\pi \int_{-\infty}^{t} f(\tau) d\tau, \tag{4.1}$$

so that $\sum_k \Delta f(k)\Delta t = \Delta\Phi/2\pi$. The value $\Delta\Phi$ that is thus obtained has an embedded Doppler shift, which we subtracted from our $\Delta\Phi$. We then find the standard deviation of 1000 samples of $\Delta\Phi$ and that is our rms phase scintillation, φ_{rms}, as shown in Fig. 4.7.

It is reasonable to expect a monotonic increase in phase scintillation with decreasing SEP angle. However, we observe departures from the expected monotonic behavior on the

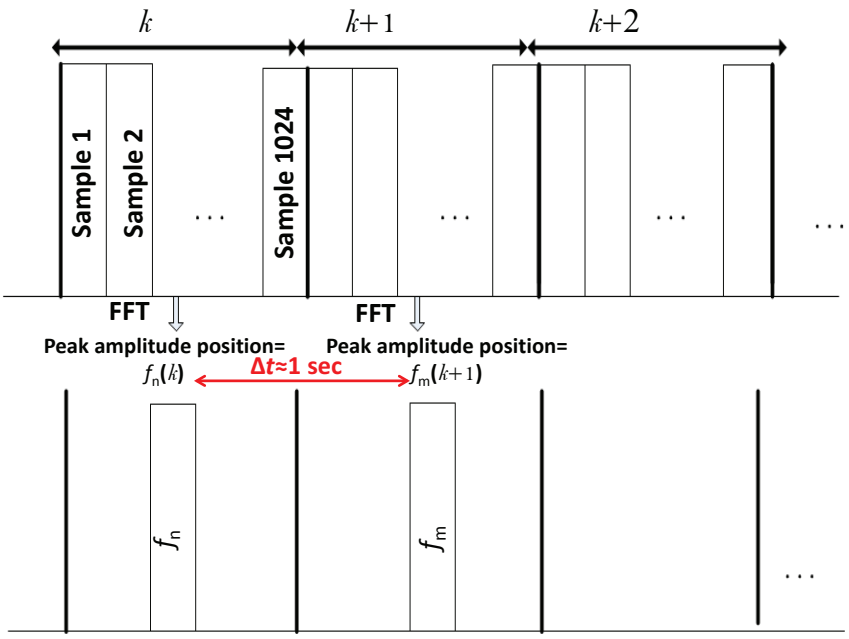

Figure 4.6: The process to find the peak bin for each 1024-point FFT.

five data sets that was obtained. We have observed two distinct characteristics for the phase scintillation depending on whether or not the phase fluctuation is sufficiently close to $\pi/2$.

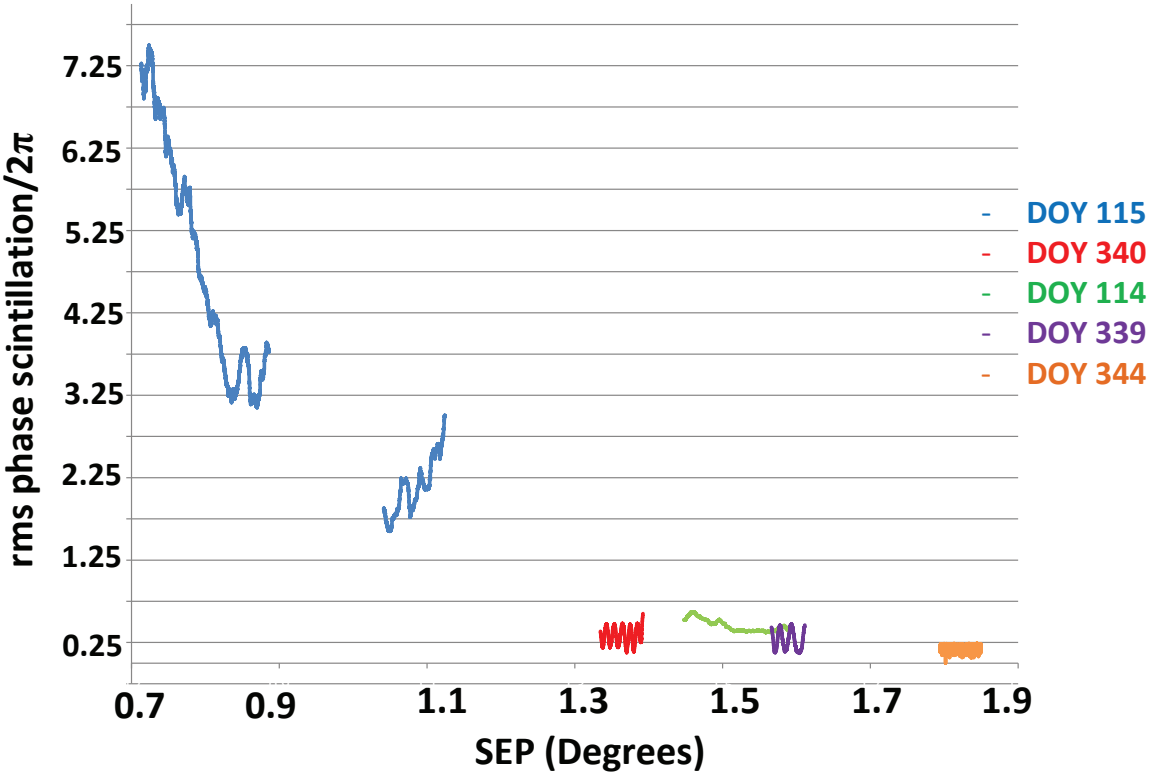

Figure 4.7: The rms phase scintillation for DOY 114, DOY 115, DOY 339, DOY 340, and DOY 344. Each data set corresponds to the SEP angle that the data was taken. When the normalized rms phase deviation approaches 0.25, 1 ± 0.25, 2 ± 0.25, ..., at which the corresponding phase deviation is an odd multiple of $\pi/2$, a deep fade of the signal strength is observed.

We attribute this behavior to phase modulation of the signal, which translates into carrier suppression when averaged over 1000 samples. In order to obtain a good carrier-to-noise ratio, the receiver has a narrow loop filter, which in our case is about 60 Hz. If after phase modulation by the turbulence, carrier power is shifted to sidebands that lie outside the loop bandwidth, then the carrier is effectively suppressed, leading to a low carrier-to-noise ratio and a poor phase estimate. To understand when we expect the carrier to be spread outside the bandwidth of the loop filter, so that carrier suppression occurs, we write the phase-modulated signal as $s(t) = A\cos\left[\omega t + \varphi(t)\right]$, where A is the signal amplitude, ω is the signal frequency, and $\varphi(t)$ is the time-varying phase. When $\varphi(t)$ varies between $+\pi/2$ and $-\pi/2$ or more generally between $+n\pi/2$ and $-n\pi/2$, where n is an odd integer, then $s(t)$ will averaged to zero, and the carrier will suppressed. In Fig. 4.8, we show the phase fluctuation for two cases. In the first case, in which the carrier is not suppressed, the rms phase fluctuation is smaller than $\pi/2$. In the second case in which the carrier is suppressed, the rms phase fluctuation is close to $\pi/2$. The carrier suppression is never complete because the phase is randomly varying. We may characterize the carrier suppression as

$$\text{carrier suppression} = 20\log_{10}\cos\left(\varphi_{\text{rms}}\right), \tag{4.2}$$

We show the carrier suppression versus φ_{rms} in Fig. 4.9, and, as shown in the figure, when φ_{rms} approaches $\pi/2$, the magnitude of the carrier suppression (fade) becomes larger. Therefore, the proximity of $\pi/2$ relates to the depth of the carrier suppression. For example, as shown in Fig. 4.9, a carrier suppression of 25 dB occurs within about 0.056 radians (3.2°) of an odd multiple of $\pi/2$, and a 1 dB carrier suppression occurs whitin 1.1 radians (63.0°). The carrier suppression plays a significant role when fluctuations of the signal-to-noise ratio becomes noticeably different from those caused by thermal noise

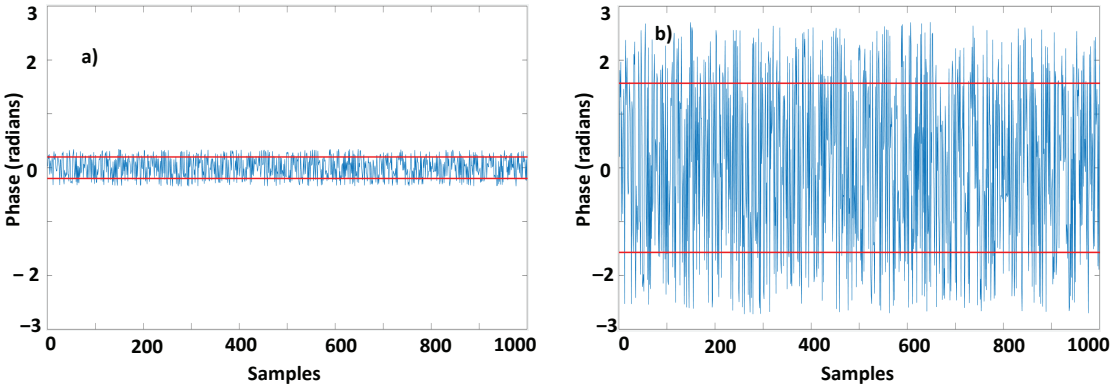

Figure 4.8: Temporal phase fluctuations (a) when the carrier is not suppressed and (b) when the carrier is suppressed. The red lines represent the rms phase deviation, φ_{rms}, of phase fluctuations averaged over 1000 samples and its negative.

alone. Fluctuations of the thermal noise are dependent on the solar elongation angle, solar activity, and also receiver noise figure. So, it is not possible to predict exactly how close to an odd multiple of $\pi/2$ the average phase fluctuation must be for the carrier to be suppressed sufficiently for the receiver to lose its phase lock. However, as we noted, the effects of losing lock are clearly visible in the data.

In conclusion, we attribute the non-monotonic behavior in Fig. 4.7 to this extrinsic effect. When the φ_{rms} caused by the intrinsic solar scintillation is at or near an odd multiple of $\pi/2$, the carrier is suppressed at the receiver. The receiver's own noise then plays an increasingly important role in determining the carrier-to-noise ratio, P_c/N_0. Because a degradation of P_c/N_0 produces a poorer phase estimate, we see larger fluctuations at $(n \pm 1/2)\pi$, where $n = 0, 1, 2, \ldots$.

Another way to analyze the data is to examine the number of occurrences and the cumulative distribution function of the carrier fade depth, as shown in Fig. 4.10. The fade depth is obtained by subtracting the maximum P_c/N_0 from P_c/N_0 for each data set and then calculating a histogram of the frequency of occurrence of the fade depth with a bin

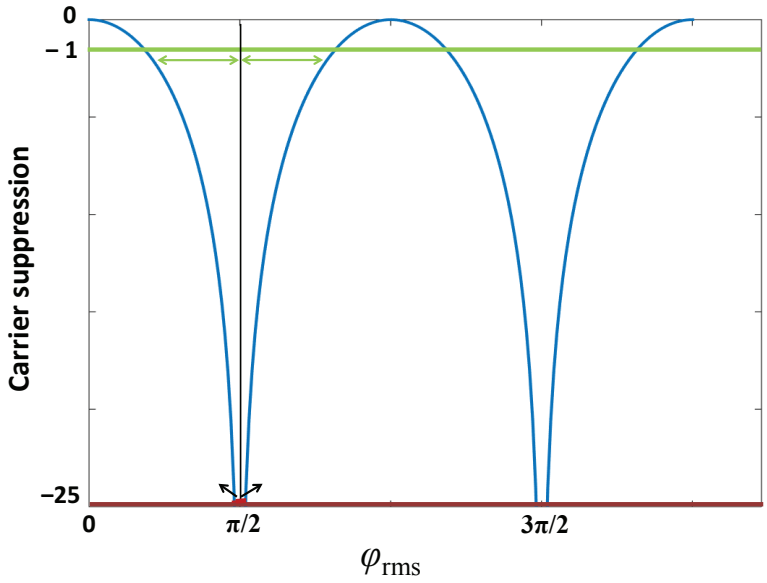

Figure 4.9: Carrier suppression vs φ_{rms}. As the angle φ_{rms} approaches an odd multiple of $\pi/2$, the carrier suppression increases.

size of 1 sec. The green line corresponds to the case in which the carrier is not suppressed. We note that the green line, corresponding to DOY 114, has a lower SEP, but it has a lower fade depth than the dark-red line, corresponding to DOY 344. In the DOY 344 data, the carrier is suppressed, and the fade depth is larger but has a lower fade probability. The pink line shows data that is obtained from DOY 98, 2015 from MESSENGER. The SEP angle for DOY 98 is almost the same as DOY 344, but the depth fade of DOY 98 is smaller, which is due to differences in solar activity. Due to solar activity, the carrier is no longer suppressed. The solar activity for DOY 114, 344 from 2014 and DOY 98 from 2015 is shown in Fig. 4.11. Solar activity can transform a carrier that is not suppressed to one that is.

We have also obtained the phase scintillation spectral density, and we observed two distinct characteristics for the phase scintillation spectral density, depending on whether the carrier is suppressed or not, as shown in Figs. 4.12 and 4.13. The phase scintillation

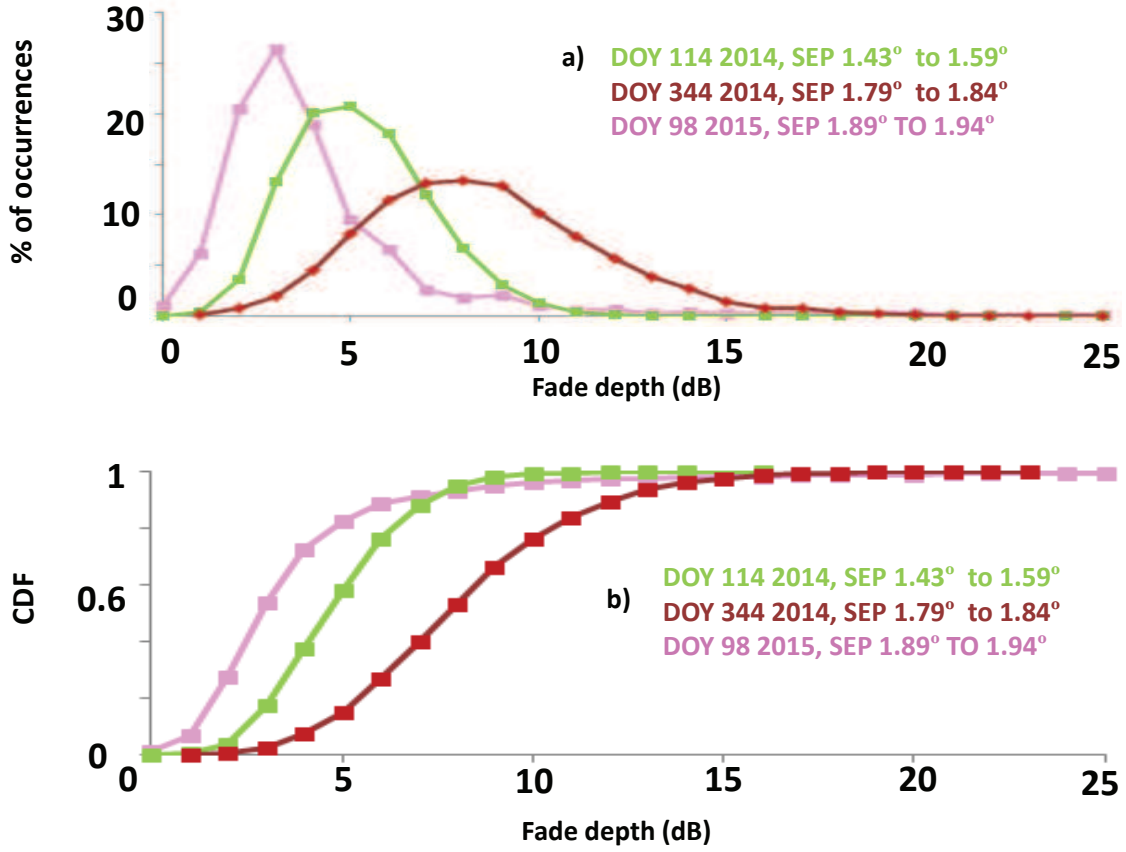

Figure 4.10: (a) The percentage of the occurrence of fade depth within a bin size of 1 Hz. (b) The corresponding cumulative distribution function.

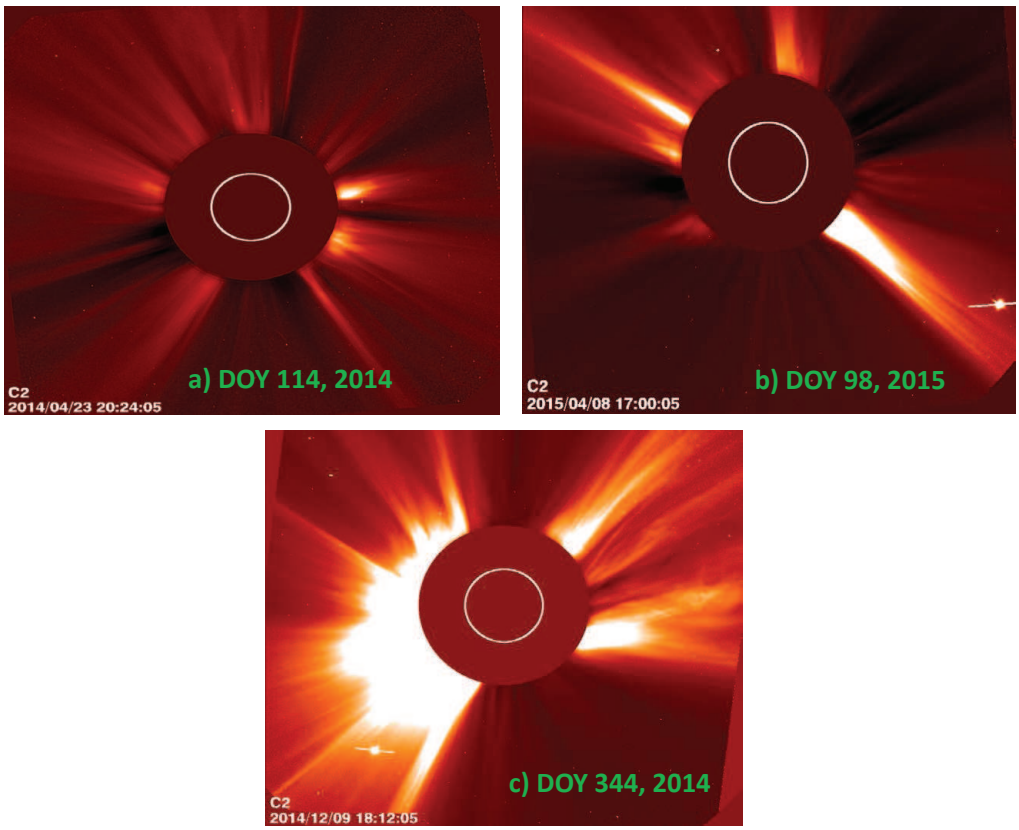

Figure 4.11: Solar activity for DOY 114 and 344 from 2014 and DOY 98 from 2015. These images were obtained by the NASA Solar and Heliospheric Observatory (SOHO) (26). The small white object seen in DOY 98 and 344 is the MESSENGER spacecraft.

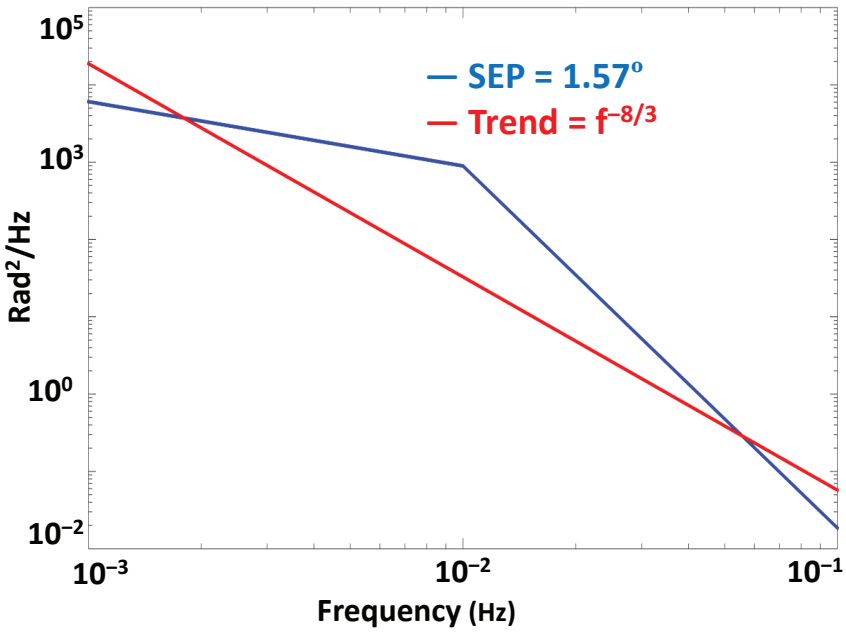

Figure 4.12: Phase scintillation spectra for DOY 114.

spectral density when the carrier is not suppressed is consistent with a Kolmogorov process for which the frequency dependence is proportional to $f^{-8/3}$, as shown in the trend line in Fig. 4.12. This result is in agreement with prior investigations by Morabito (23) and Imamura (24). However for a carrier-suppressed condition, the receiver noise obscures the underlying turbulent process and produces dependence that is proportional to f^{-1}, as shown in Fig. 4.13, corresponding to the f^{-1} flicker noise of the receiver.

4.7 Amplitude Scintillation

Inspection of the 1024-point FFT indicates that sideband power was confined to 10 bins on either side of the carrier. Beyond that, any sideband power is obscured by antenna thermal noise. Because the time duration of each FFT is 1.024 seconds, we conclude that any modulation due to the solar corona has an upper bound of approximately 10 Hz. Moreover, we determined that the upper and lower side bands are symmetrical about the

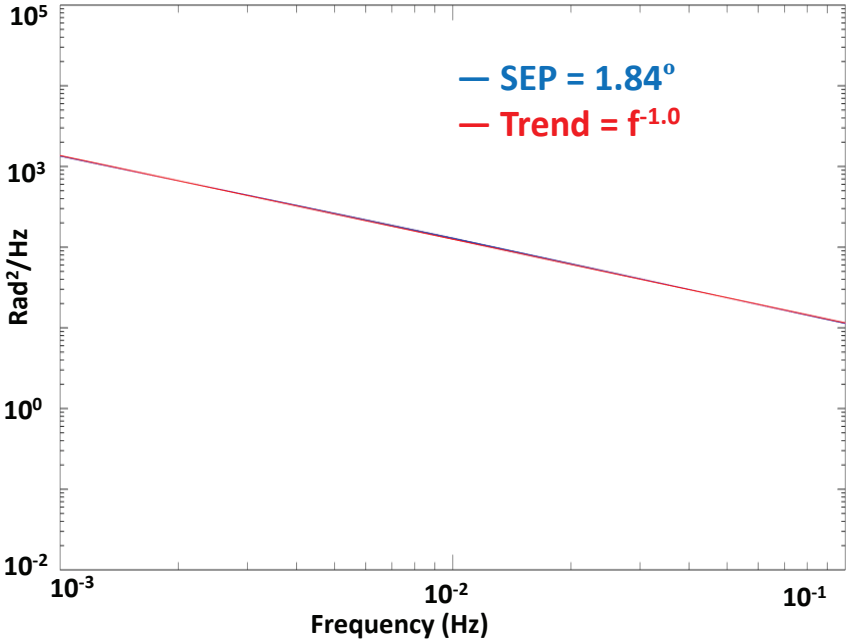

Figure 4.13: Phase scintillation spectra for DOY 344.

carrier, and hence the modulation on this time scale is predominantly due to amplitude modulation.

The strength of the sidebands depends on how amplitude modulation (AM) and phase modulation (PM) are combined. For 100% amplitude modulation, we expect that the lower side band (LSB) and upper side band (USB) are symmetrical, i.e., they have the same amplitude and phase. Phase modulation causes the sidebands to be out of phase. So, the combination of both causes the spectrum to be asymmetrical, as shown schematically in Fig. 4.14.

The power in the LSB and the USB is obtained by averaging the summation of the squared amplitude of 10 bins from the left and right side respectively of the peak power. Analysis of the sidebands from our data indicates: 1) The ratio of the powers in the sidebands for DOY 115 are higher than for DOY 114, as shown in Figs. 4.15 and 4.16, which indicates that the scintillation effects on the sideband power increase as the SEP angle de-

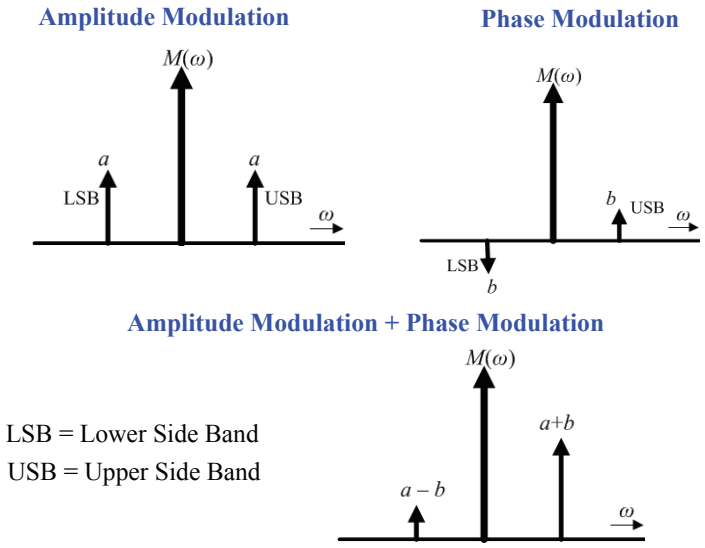

Figure 4.14: Different Modulation Schemes.

creases. 2) Linear regressions for both data sets show a negative slope as expected, which again indicates that the power in the sidebands increases as the SEP angle decreases. In order to know the exact ratio of the amplitude modulation to phase modulation, one must compare the amplitude and phase for each bin from LSB and USB. Since some bins were dominated by noise, we compare the square root of the LSB and USB power for DOY 115. The ratio of PM to AM for USB vs. LSB is $(\mathrm{AM}+\mathrm{PM})/(\mathrm{AM}-\mathrm{PM}) = 1.11$, which corresponds to a 95% amplitude modulation and a 5% phase modulation. These results imply that on a time scale of one second our data is dominated by amplitude modulation. Therefore, we calculated the scintillation index, assuming that our data is amplitude modulated as we explain next.

The scintillation index is a measure of the degree of fluctuation that a signal's amplitude experiences due to passage through the small-scale plasma irregularities in the corona. The scintillation index is defined as the rms of the received intensity fluctuations divided by the mean intensity. It can be calculated from a measured time series of the signal strength

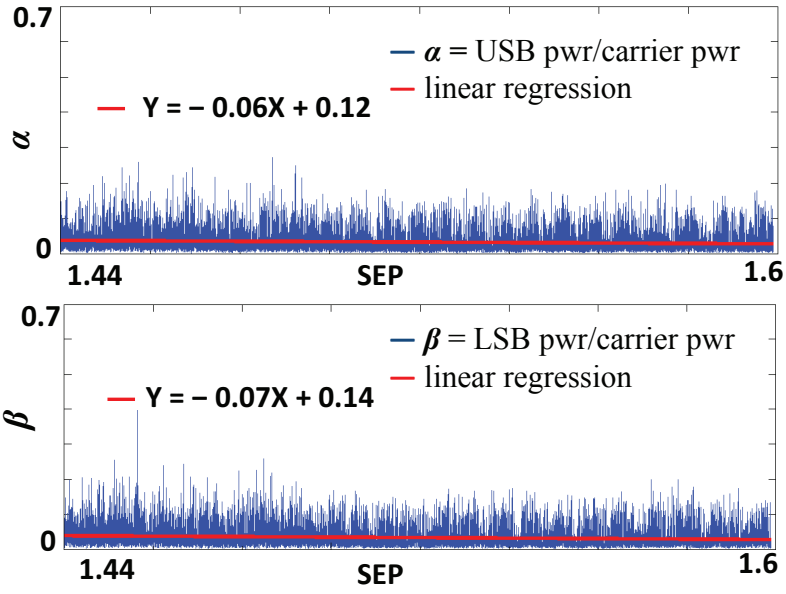

Figure 4.15: DOY 114; Ratio of USB power and LSB power to carrier power vs. SEP angle.

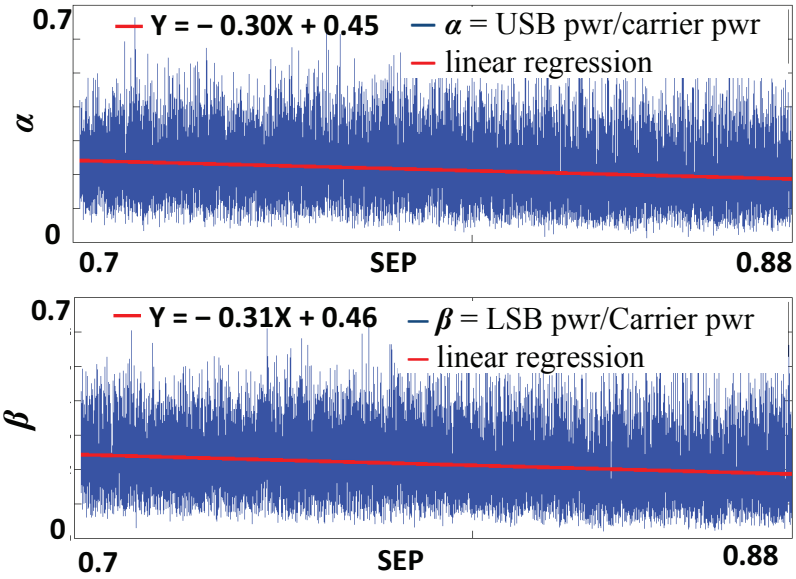

Figure 4.16: DOY 115; Ratio of USB power and LSB power to carrier power vs. SEP angle.

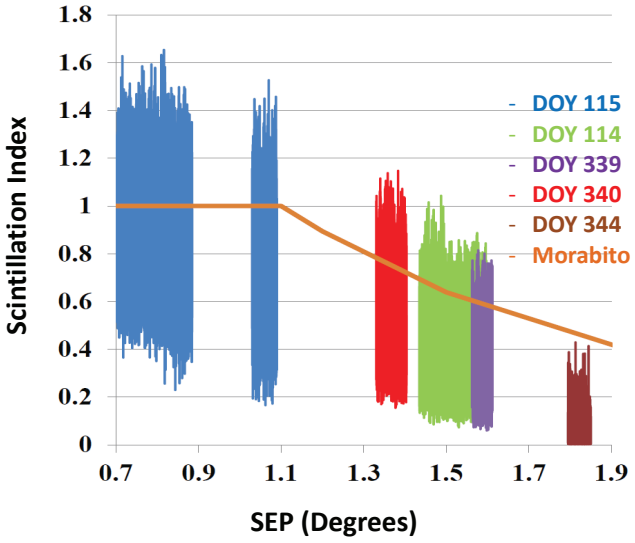

Figure 4.17: Amplitude scintillation index on a 1 sec time scale.

as the ratio of the rms of the received power fluctuations relative to the mean power over the observation interval. Since our sideband power is dominated by amplitude modulation, the root-mean square (rms) of the received intensity fluctuations is the rms of the received power from both sidebands (25),

$$Ps = \frac{|mA|^2}{2}, \tag{4.3}$$

where m is the scintillation index. The mean intensity is the carrier power,

$$Pc = \frac{1}{2}|A|^2. \tag{4.4}$$

The scintillation index averaged over one second is shown in Fig. 4.17, and the results have been compared to the theoretical model of Morabito (23). As shown in Fig. 4.17 our results and Morabito's follow the same trend, and the index of refraction reaches saturation when the SEP angle is about 1.1°.

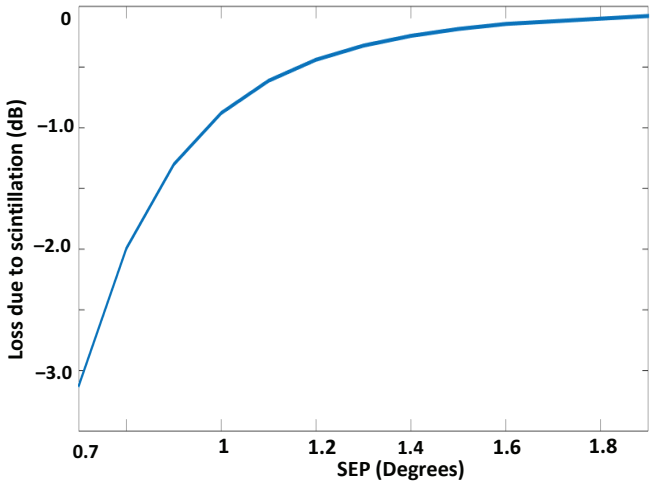

Figure 4.18: Loss due to amplitude scintillation index vs. SEP angle.

4.8 Loss due to Amplitude and Phase scintillation

The power from the carrier signal is transferred to the sidebands due to scintillation. Therefore, the sideband power contributes to amplitude scintillation loss, but this loss is not an additive loss; instead, it is a multiplicative loss. Hence, we cannot improve the performance of the carrier by increasing the carrier power. We can write the loss due to amplitude scintillation as

$$L_s = \frac{Pc - Ps}{Pc} = 10\log\left(1 - \frac{m^2}{2}\right). \tag{4.5}$$

As shown in Fig. 4.18, the loss to the sidebands is 3 dB when the SEP angle equals 0.7°. At this angle, half of the carrier power goes into the sidebands regardless of the carrier power level since this loss is multiplicative.

Analysis of these data indicate that on a one-second time scale, the signal fluctuations are dominated by amplitude scintillation. This finding is consistent with Morabito (23) and Imamura (24). However, amplitude scintillation does not tell the whole story. Indeed, the

data on DOY 344, which exhibits a lower amplitude scintillation than predicted by Morabito's theoretical model, had severe carrier fading over the entire data duration. Moreover, the severity and frequency of occurrence of this fading was worse compare to DOY 114 as shown in Fig. 4.10, even though it has a larger SEP angle. As shown in Fig. 4.10 (b) for DOY 344, the probability of a 10 dB fade is about 50 percent, which is due to phase scintillation. This behavior is explained in the next section.

Chapter 5

Solar scintillation study during planetary conjunction: Theoretical study

5.1 The Sun's dynamic atmosphere and plasma

We analyzed recent data obtained during superior solar conjunction of MESSENGER at X-band for days 114, 115, 339, 340, and 344, during which SEP angle varied between 0.7° to 1.84°. We observed a short time-scale and a long time-scale effect. On a short time scale of one second, the amplitude scintillations dominate. On a long time scale of hundreds to thousands of seconds, the phase scintillations dominate. Prior to our work, there was no physical explanation for why there are two different time scales for these observations.

The rapid amplitude scintillations are due to scattering from the rapidly changing index of refraction in the solar wind. The slower phase scintillations are harder to explain. We investigated several possible phenomena that explain the slow phase scintillations. We found that long-lasting solar wind ducts could explain this behavior. Other possibilities that we considered were propagation through seperate clouds of protons and electrons, changes in the index of refraction due to supersonic particles, and separation of electrons and protons due to inhomogeneous magnetic fields, leading to changes in the index of refraction.

We found that these other possibilities, could not explain the slow phase scintillations. We begin by reviewing the physics of the Sun's atmosphere and the plasma that surrounds it. The outer layer of the Sun near its surface is like a pot of boiling water, with bubbles of hot electrons and protons in a fourth state of matter known as the plasma state. This plasma circulates up from the interior of the Sun and bursts out into space (27). The steady stream of particles blowing away from the Sun is known as the solar wind. The solar wind varies in density, temperature, and speed as a function of time and the solar longitude. Its particles can escape the Sun's gravity because of their high energy. The solar wind plasma consists of mostly electrons, protons and alpha particles.

A useful definition for a plasma follows: A plasma is a quasineutral gas of charged and neutral particles that exhibits collective behavior (28). By collective behavior, we mean that the motion of the particles not only depends on interactions with nearby particles and external fields, but it also depends on the state of the plasma, which is determined by long-range interactions among all the particles. As charges move around, they can generate local concentrations of positive or negative charge, which give rise to electric fields. Motion of charges also generate currents and hence magnetic fields. These fields affect the motion of other charged particles far away. Therefore, the electron and proton charges of a plasma exert a force on one another even at large distances. It is these long-range forces that give the plasma a large repertoire of possible behaviors (28).

In order to investigate the origin of the two different time scales for amplitude scintillations and phase scintillations, we will focus on the physics of single-component plasmas, including the energy distribution of the charged particles that make up each component and the separation between different components.

5.2 Debye length in solar plasma

The Debye length (λ_D) is the minimum distance over which a plasma can exhibit collective behavior. For plasma phenomena that occur on length scales that are less than λ_D, the ions and electrons can be treated as individual particles. The length scales for electrons and protons are given by (29)

$$\lambda_{De} = \left(\frac{\varepsilon_0 K_B T_e}{N_e e^2} \right)^{1/2} \tag{5.1}$$

and

$$\lambda_{Dp} = \left(\frac{\varepsilon_0 K_B T_p}{N_p e^2} \right)^{1/2}, \tag{5.2}$$

where ε_0 is the permittivity of free space, K_B is the Boltzmann constant, T_e and T_p are the electron and proton temperature, N_e and N_p are the electron and proton density and e is the absolute value of the electron charge. In Fig. 5.1, we show Debye lengths for electrons and protons that are based on the fast solar wind temperature and density defined in (30) and (31). The data on electron and proton temperature and density is provided by the Solar Probe Plus Science team at the Johns Hopkins University Applied Physics Laboratory (unpublished). Many of our results are functions of the solar radius, R_s. The relation between R_s and the SEP angle is shown in Fig. 5.2.

The Debye length of the protons is longer than the electrons, as shown in the Fig. 5.1. As mentioned above, the density of electrons and protons are constantly changing, and the solar wind is dynamic. While Fig. 5.1 shows data for a fast solar wind, a similar difference in Debye length exists for a slow and average solar wind. The degree to which collective

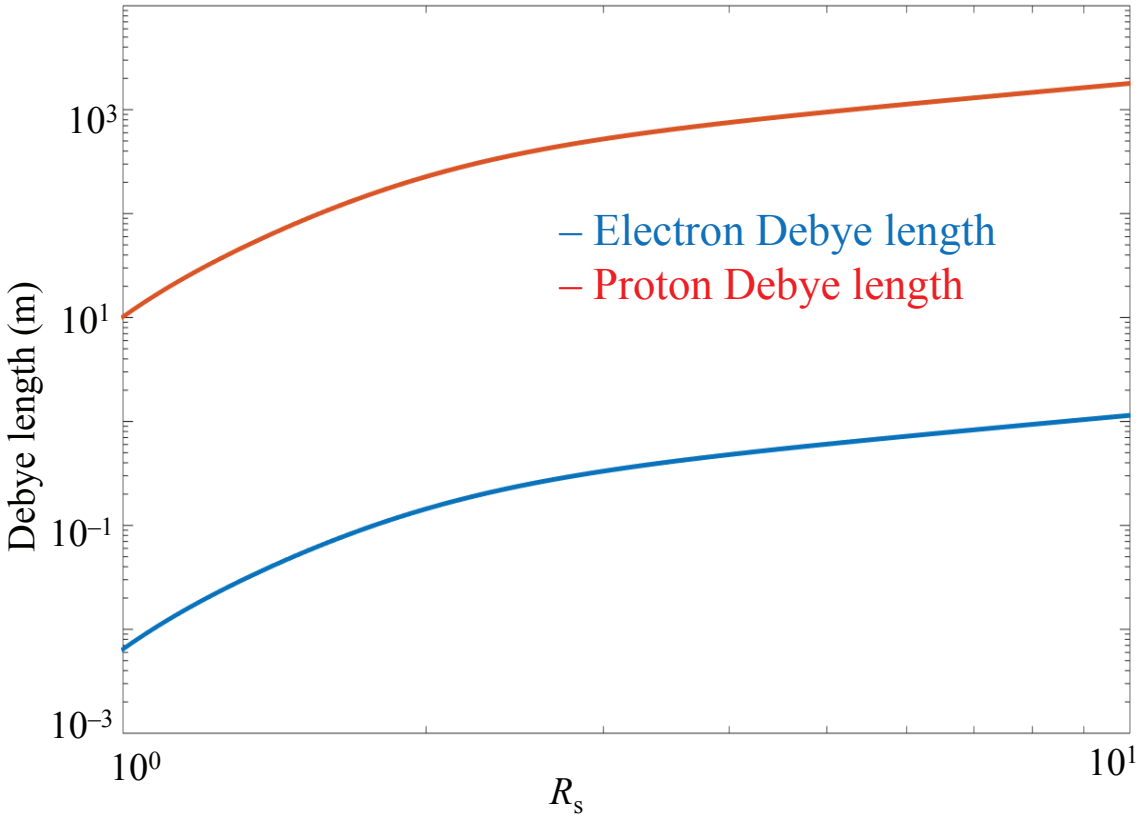

Figure 5.1: Electron and proton Debye lengths as a function of the solar radius for the fast solar wind.

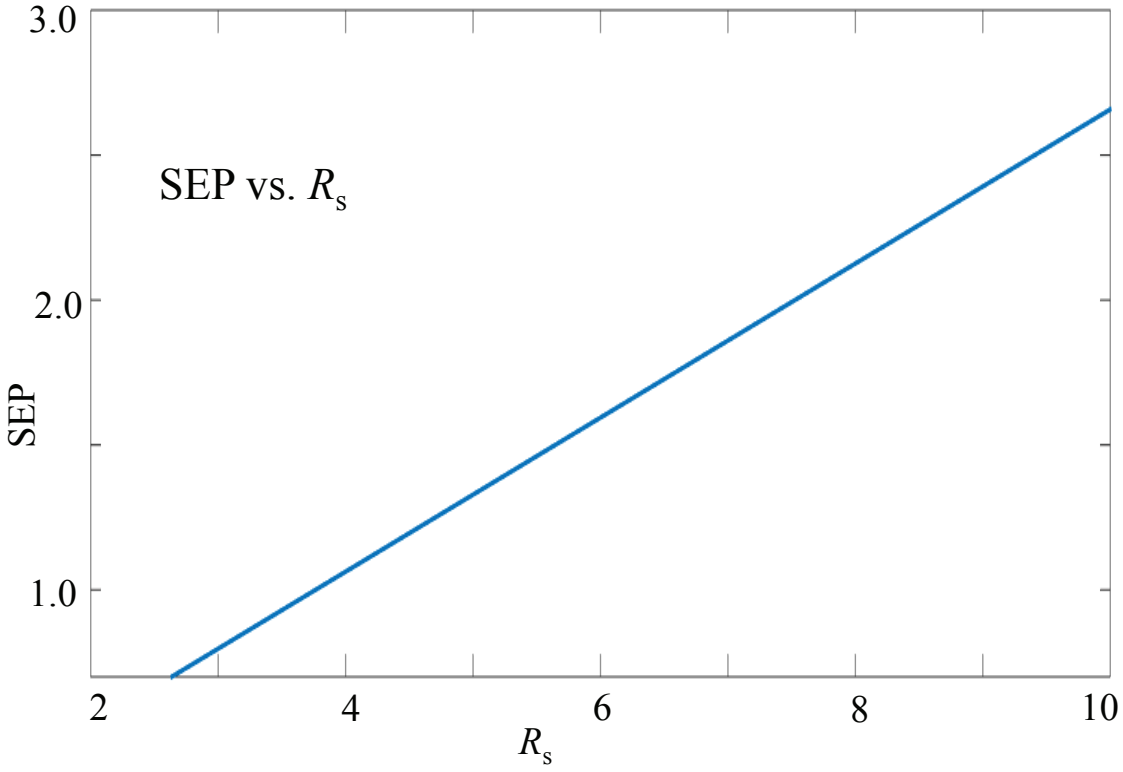

Figure 5.2: SEP angle vs. solar radius

behavior occurs is determined by the number of plasma particles in a Debye sphere ($N_{\lambda D}$),

$$N_{\lambda D} = \frac{4\pi}{3}\lambda_D^3 N_e. \tag{5.3}$$

When this number is much greater than unity, collective behavior dominates. In our case the number of particles in a Debye sphere is much greater than unity.

In order to explain the amplitude scintillations, it is important to look at the ratio of the RF beam wavelength to the Debye length scale. The RF X-band wavelength is 0.0375 m. The scale of the Debye length for electrons is smaller than the X-band wavelength at closest approach to the Sun. Therefore, the amplitude scintillations are caused by scattering of the RF beam as it propagates through the clouds of electrons. However, as we previously noted, this scattering does not explain the phase scintillations and its time scale. In order to do that, we will first study the impact on the index of refraction of the separation between the electrons and the protons.

5.3 Index of refraction in solar plasma

We begin with the equation of motion of an electron in an applied electric field, $\mathbf{E}(t) = \mathbf{E}_o \exp(-i\omega t)$, where $\omega = 2\pi f$ and f is the radiation frequency, which in this case is the X-band RF wave frequency (32),

$$m\frac{d^2\mathbf{x}}{dt^2} = -e\mathbf{E}_o \exp(-i\omega t) - m\nu_c\frac{d\mathbf{x}}{dt}, \tag{5.4}$$

where $\mathbf{x}$ is the electron displacement from its neutral position, m is the electron mass and ν_c is the collision frequency of electrons with the gas molecules. The steady-state solution must vary as $\exp(-i\omega t)$ and is

$$\mathbf{x} = \frac{e/m}{\omega^2 + i\nu_c\omega} E_o \exp\left(-i\omega t\right). \tag{5.5}$$

We note that [(32), Eq. 5.2.9] is mistaken and predicts an index of refraction that is less than one. However, we will show that the index of refraction in an ionized medium is always greater than one. In order to compare our results to (32), we use cgs units in this section.

The electric displacement **D** is given by

$$\mathbf{D} = \mathbf{E} + 4\pi\mathbf{P}, \tag{5.6}$$

where **P** is the polarization density. The electric displacement is also related to the electric field as $\mathbf{D} = \epsilon\mathbf{E}$, where ϵ is the permittivity, and we assume that **P** is linearly proportional to **E**. Therefore, we can write Eq. 5.6 as

$$\epsilon = 1 + 4\pi\frac{|\,\mathbf{P}\,|}{|\,\mathbf{E}\,|}. \tag{5.7}$$

The polarization density is related to the electron displacement,

$$\mathbf{P} = Ne\mathbf{x}, \tag{5.8}$$

where N is the number of charge dipoles per unit volume in the ionized plasma or ion density. By substituting Eq. 5.5 and Eq. 5.8 into Eq. 5.7, we obtain

$$\epsilon = 1 + \frac{\omega_e^2/\omega}{\omega + i\nu_c} = 1 + \frac{\omega_e^2}{\omega}\frac{\omega - i\nu_c}{\omega^2 + \nu_c^2}, \tag{5.9}$$

where $\omega_e^2 = 4\pi Ne^2/m$ is the plasma frequency. The real part of Eq. 5.9 is related to the index of refraction. Therefore the index of refraction for the RF wave with $\mu = 1$ and

$\nu_c \ll \omega$ is

$$n = \frac{kc}{\omega} = \left(1 + \omega_e^2/\omega^2\right)^{1/2}. \tag{5.10}$$

Equation 5.10 implies that the index of refraction is always greater than unity. In Fig. 5.3, we show the indices of refraction for the electron and proton as the RF wave propagates through them. The RF wave experiences different indices of refraction due to the mass differences between electrons and protons. As the RF wave propagates further from the Sun, the indices of refraction approach unity for both the electron and the proton, since the plasma frequency gets very small, which also indicates that the effect of plasma on the RF beam gets weaker.

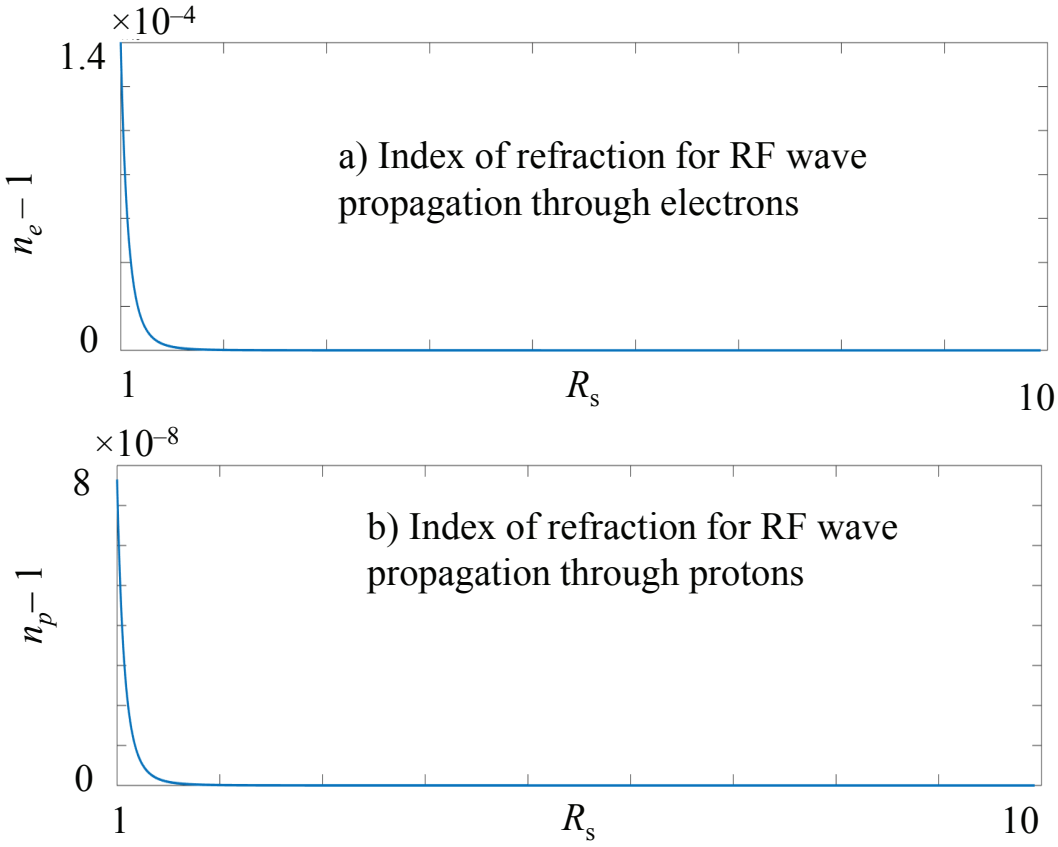

Figure 5.3: Index of refraction for (a) electrons and (b) protons.

5.4 Investigation of possible sources of the long-time phase scintillations

We have investigated four phenomena that exist in the solar wind and that could potentially explain the long-time phase scintillations.

We first investigated the propagation of radio waves in the positively and negatively charged clouds of protons and electrons that are approximately a Debye length in size. The difference between the indices of refraction in these clouds will lead to phase variations in the beam wavefront as the RF beam propagates. Second, we investigated the passage of supersonic particles in acoustic waves that locally change the index of refraction, leading to phase variations in the beam wavefront as the RF beam propagates. Third, we investigated the separation of electrons and protons that are due to inhomogeneous solar magnetic fields. This separation leads to local change in the indices of refraction and hence phase variations in the beam wavefront as the RF beam propagates. Fourth, we investigate ducts in the solar plasma that trap a part of the RF beam, which leads to phase variations in the beam wavefront as the RF beam propagates. We concluded that the most probable source of the long time scale of the phase scintillations is the effect of long ducts.

5.4.1 The positively and negatively charge clouds of protons and electrons effect on the RF beam

In the solar plasma, electrons and protons can be treated as individual clouds on the scale of the Debye length, as shown schematically in Fig. 5.4. We investigated the propagation of radio waves in the positively and negatively charged clouds of protons and electrons and whether the difference between the electron and proton plasma wave indices of refraction in these clouds can explain these long-time phase scintillations. To do so, we examined the propagation of a radio wave in the plasma clouds.

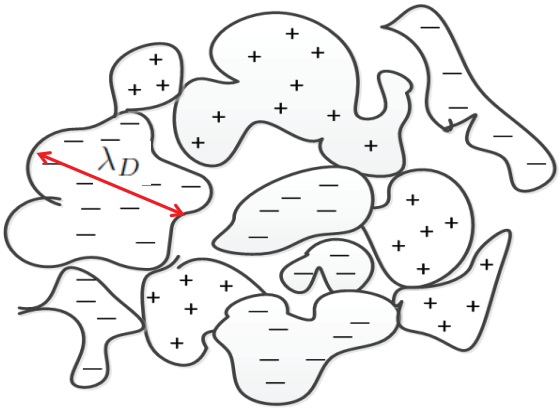

Figure 5.4: The solar wind plasma is shown schematically as patches of electron and proton clouds. These clouds are on the order of a Debye length in size.

The speed of a radio wave that propagates in these clouds of electrons and protons is respectively, c/n_e and c/n_p, where c is the speed of light, while n_e and n_p are the indices of refraction for electron and proton RF waves. The times required for radio wave to propagate through the clouds of electrons, t_e, and protons, t_p, are

$$t_e = \lambda_{De}\frac{n_e}{c} \tag{5.11}$$

and

$$t_p = \lambda_{Dp}\frac{n_p}{c}. \tag{5.12}$$

As shown in Fig. 5.5 the time t_e for the radio wave to propagate through a cloud of electrons is three orders of magnitude less than the time t_p for it to propagate through a cloud of protons. However, the propagation time t_e for electrons varies between nanoseconds and microseconds, which is far smaller than the time scale of hundreds to thousands of seconds that we have observed in the phase scintillations. Hence, this effect cannot explain the long-time phase scintillations.

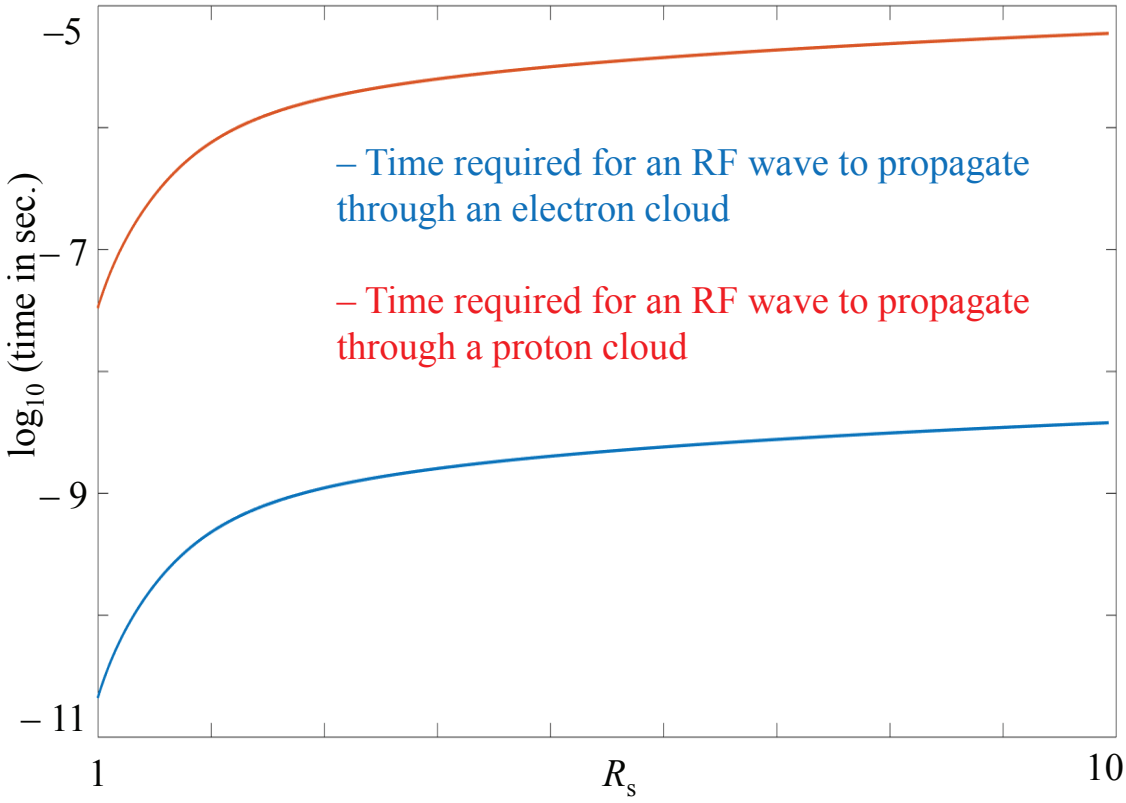

Figure 5.5: Time required for RF wave to propagate through electron patch versus proton patch

5.4.2 Passage of supersonic particles in acoustic waves and their effect on the RF beam

Sound waves escaping the Sun's interior create fountains of hot gas that shape and power the chromosphere. They create a thin region in the Sun's atmosphere that appears as a red ring of fire (33). Ion acoustic waves in plasmas are frequently referred to as acoustic waves or as sound waves. Acoustic waves are one type of longitudinal oscillation of the ions and electrons in a plasma, much like acoustic waves traveling in a neutral gas. The acoustic wave speed can be written as (34)

$$v_{ac} = \sqrt{\frac{K_B(\gamma T_p + T_e)}{m_p}}, \tag{5.13}$$

where K_B is the Boltzmann constant, T_e and T_p are the electron and proton temperature, γ is the specific heat capacity ratio and m_p is the proton mass. As shown in Fig. 5.6, the ion acoustic speed decreases at distances that are further from the Sun, as expected.

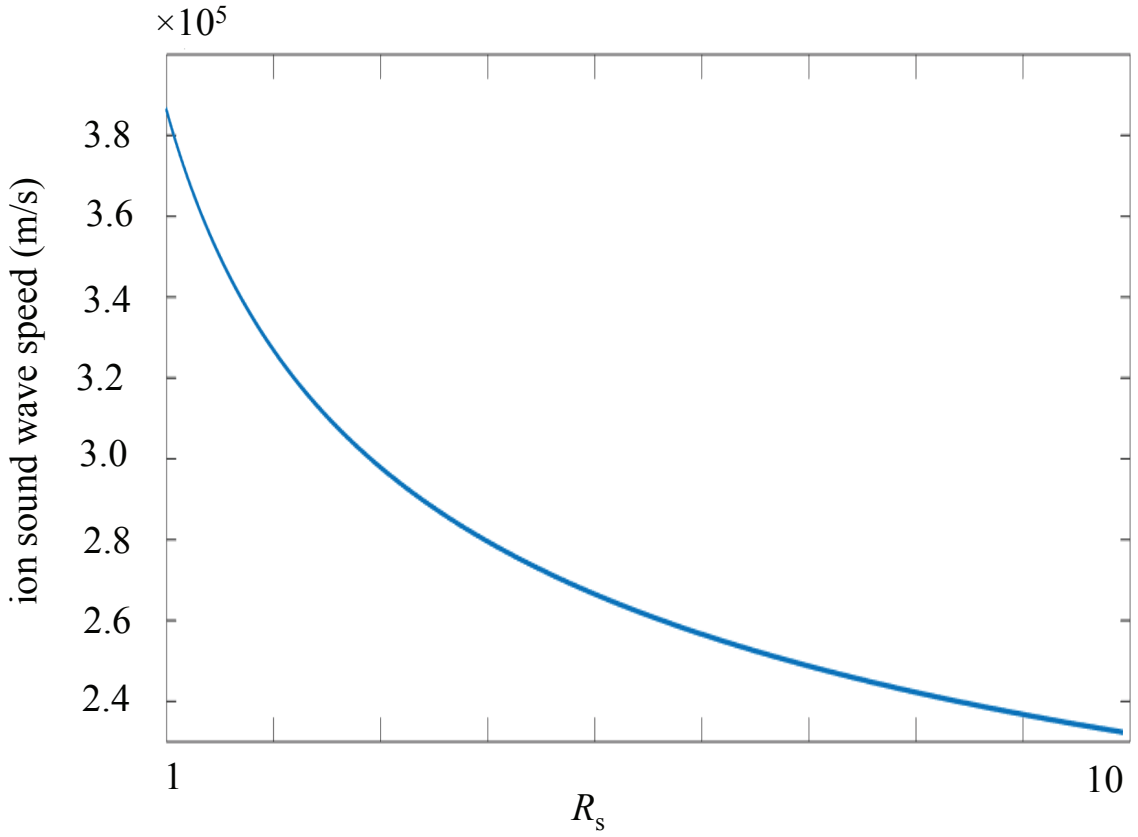

Figure 5.6: The speed of the ion sound wave decreases further from the Sun.

In the solar plasma, supersonic waves are constantly entering into the plasma, due to eruptions on the surface of the Sun. Solar flares and coronal mass ejections (CME) both generate supersonic waves (35).

When supersonic waves travel, the density, velocity, and pressure change across the

shock. The index of refraction is related to the charge density as shown in Eq. 5.10. Therefore, changes in density across the shock cause the index of refraction to also change. We investigated the passage of supersonic particles through an acoustic wave that locally changes the index of refraction, leading to phase variations in the beam wavefront as the RF beam propagates.

The ion acoustic wave velocity, shown in Fig. 5.6, is 3.8×10^5 m/s at closest approach to the Sun. This velocity is smaller than the velocity of solar flares, 2.99×10^8 m/s, and CMEs, 4.4×10^5 m/s (35). When the particles in solar flares and CMEs are moving faster than the local acoustic velocity, they create a shock wave (34). The change of the density across the front of a shock wave, N_2, is (34)

$$N_2 = \frac{(\gamma+1)M_1^2}{2+(\gamma-1)M_1^2} N_1, \tag{5.14}$$

where N_1 is the density of the acoustic waves and M_1 is the Mach number. The Mach number is the ratio of the particle speed to the acoustic speed. The heat capacity ratio, γ, for an ideal gas is 1.4. In both solar flares and CMEs, the Mach number $M_1 \gg 1$, so that Eq. 5.14 reduces to

$$\frac{N_2}{N_1} = \frac{\gamma+1}{\gamma-1} = 6. \tag{5.15}$$

Therefore, the maximum change in density that exists across the shock waves is $6N_1$. From the Clausius-Mossotti equation, we obtain the relation of the index of refraction to the number density (36),

$$\frac{n^2-1}{n^2+2} = \frac{1}{3\epsilon_0} N\alpha, \tag{5.16}$$

where N is the number density, n is index of refraction, α is the polarizability, and ϵ_0 is the permittivity of the vacuum. We let $K = (1/3\epsilon_0)N\alpha$, and at one solar radius we obtain

$K \sim 6.2 \times 10^6$. The index of refraction of the sound waves may be written

$$n^2_{\text{sound}} = \frac{2K+1}{1-K}, \tag{5.17}$$

and the index of refraction of the shock waves may be written

$$n^2_{\text{shock}} = \frac{12K+1}{1-6K}. \tag{5.18}$$

Therefore, the ratio of the indices of refraction becomes

$$\frac{n^2_{\text{shock}}}{n^2_{\text{sound}}} = \left(\frac{12K+1}{2K+1}\right)\left(\frac{1-K}{1-6K}\right). \tag{5.19}$$

We concluded that $n_{\text{shock}} \simeq n_{\text{sound}}$. This result also is consistent with Eq. 5.10. The second term in the index of refraction is dominated by the RF beam frequency, so that increasing the density by a factor of 6 will not make a significant change to index of refraction. Hence, this effect cannot cause phase scintillations on the time scale of hundreds to thousands of seconds that we have observed in our data.

5.4.3 Charge separation due to an inhomogeneous magnetic field

Electric currents inside the Sun generate a magnetic field that spreads throughout the solar system. A solar wind composed of charged particles carries the magnetic field away from the Sun's surface and through the solar system. The Sun's magnetic influence extends well past the planets and into interstellar space (27).

The magnetic moment of electrons, the Bohr magneton (μ_B), is a factor of 1836 larger than the magnetic moment of protons. Also, the force on an electron for a given gradient of the magnetic field, is stronger than the force on a proton. The electron is a factor of 1836

lighter than the proton. Thus, acceleration of electrons is a factor of 1836^2 stronger than the acceleration of protons.

We investigated the separation of electrons and protons that is due to inhomogeneous solar magnetic fields. This separation leads to local change in the indices of refraction and hence phase variation in the beam wavefront as the RF beam propagates.

To investigate this possibility we must compare the two dipole forces that a charged particle experiences due to the magnetic field gradient. The first dipole force is due to the Larmor motion or gyro-motion of the particle in a magnetic field. The second dipole force is due to the Bohr magneton.

The force on a charged particle in a magnetic field gradient is given by,

$$\mathbf{F} = \nabla \left(\mu \cdot \boldsymbol{B} \right). \tag{5.20}$$

where F is the external force, μ is the magnetic dipole moment and B is the applied magnetic field. For simplicity, we assume the gradient of the magnetic field only changes in the z-direction as shown in Fig. 5.7. Therefore, the force due to the Bohr magneton on an electron and on a proton becomes

$$F_{Be} = \mu_{Be} \left(\frac{\partial B_z}{\partial z} \right), \tag{5.21}$$

and

$$F_{Bp} = \mu_{Bp} \left(\frac{\partial B_z}{\partial z} \right), \tag{5.22}$$

where μ_{Be} and μ_{Bp} are the magnetic dipole moments for the electron and protons respectively. The Bohr magnetic moment for a charge particle is

$$\mu_B = \frac{e\hbar}{2m}, \tag{5.23}$$

where e is the elementary charge, $\hbar$ is the reduced Plank constant, m is the rest mass of the electron or proton. The Bohr magneton for an electron is $\mu_{Be} = 0.58$ eV/G and for a proton is $\mu_{Bp} = 3.1 \times 10^{-4}$ eV/G.

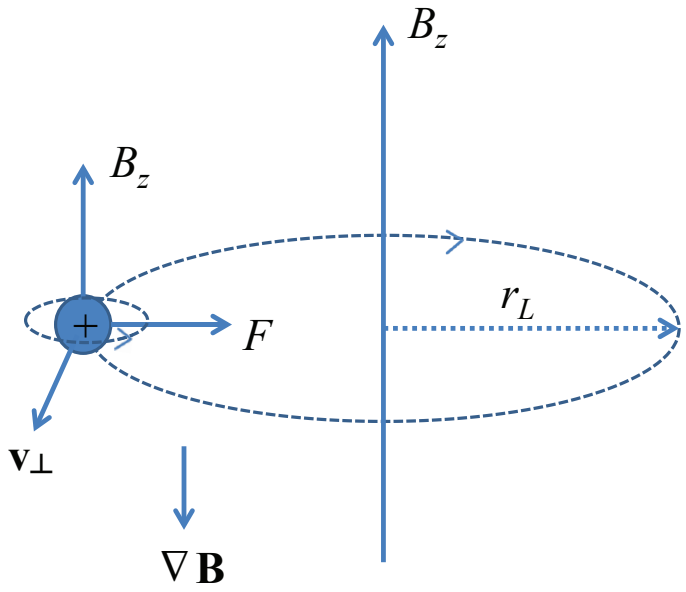

Figure 5.7: The spin and gyromotion of a charged particle in the presence of a magnetic field gradient.

The charged particle also experiences a gyro-motion. The corresponding Larmor dipole moment is

$$\mu_L = \frac{mv_\perp^2}{2B}, \tag{5.24}$$

where $v_\perp$ is the speed of the particle. We may write $mv_\perp^2/2 = W_\perp$, where $W_\perp$ is the perpendicular kinetic energy of the charged particle. The Larmor forces, acting on the

electrons and protons, F_{Le} and F_{Lp} respectively, are

$$F_{Le} = \left(\frac{W_{\perp e}^2}{B}\right)\left(\frac{\partial B_z}{\partial z}\right) \tag{5.25}$$

and

$$F_{Lp} = \left(\frac{W_{\perp p}^2}{B}\right)\left(\frac{\partial B_z}{\partial z}\right). \tag{5.26}$$

In Fig. 5.7, we show a schematic illustration of these forces.

We now write the perpendicular kinetic energy as $W_{\perp e} = K_B T_e$ and $W_{\perp p} = K_B T_p$, since $K_B T$ is the kinetic energy. Therefore, the ratio of the forces due to the Bohr magneton magnetic moment and the Larmor magnetic moment is

$$\frac{F_{Be}}{F_{Le}} = \frac{\mu_{Be} B}{K_B T_e} \sim \frac{(0.6\text{eV/G})(1G)}{100\text{eV}} \ll 1 \tag{5.27}$$

for an electron. The ratio of forces is

$$\frac{F_{Bp}}{F_{Lp}} = \frac{\mu_{Bp} B}{K_B T_p} \sim \frac{(3\times 10^{-4}\text{eV/G})(1G)}{100\text{eV}} \ll 1 \tag{5.28}$$

for a proton. Therefore, thermal motion dominates the charged particle motion, and inhomogeneity in the solar magnetic fields cannot cause a significant charge separation.

5.4.4 Plasma ducting effect on the RF beam

The influence of atmospheric refraction on the propagation of electromagnetic waves has been studied from the beginning of radio wave technology (37). The path bending of electromagnetic waves due to an inhomogeneous spatial distribution of the refractive index can cause adverse effects such as multipath fading and interference. These effects significantly impair radio communication, navigation, and radar systems. Atmospheric refractiv-

ity is dependent on physical parameters of the air such as its pressure and temperature. It varies in space and time due to physical processes in the atmosphere that are often difficult to describe in a deterministic way and have to be, to some extent, considered as random with its probabilistic characteristics (38). Atmospheric ducting is a mode of propagation of electromagnetic radiation, usually in the lower layers of the Earth's atmosphere, where the waves are bent by atmospheric refraction. In over-the-horizon radar, ducting causes part of the radiated and target-reflection energy of a radar system to be guided over distances far greater than the normal radar range (39). It also causes long distance propagation of radio signals in bands that would normally be limited to line of sight. We investigated the possibility that the same phenomenon exists in the solar wind plasma. In particular, we investigated whether an inhomogeneous spatial distribution of the refractive index can create a plasma duct in the solar plasma, so that part of the radiated plane wave is trapped in the duct on a time scale of seconds to minutes.

To address this issue we start with a simple slab model. We consider a plane wave that propagates through solar plasma and reaches a plasma duct as shown schematically in Fig. 5.8. Ducting occurs due to refraction that bends the propagation path of the RF wave as it propagates through layers of different density. Some parts of the radiated plane wave are refracted into the duct due to a change of the index of refraction. Changes of the index of refraction exist, as shown in Fig. 5.3. The index of refraction for protons is smaller than for electrons, i.e, $n_p < n_e$. When a portion of the radiated wave is trapped inside a duct, it bounces many times before exiting from the duct, as shown in Fig. 5.8. When the radiated wave leaves the duct, it can destructively interfere with radiation that was not in the duct, suppressing the carrier. As shown schematically in Fig. 5.9, an RF uplink beam can pass through many ducts before reaching Mercury. The wavefront of the beam that has traveled a length l outside the duct and the wavefront of the trapped beam that has traveled a length $\sqrt{l^2 + d^2}$ inside the duct, interfere with each other. When the phases of the two wavefronts

differ by an odd number of half wavelengths, so that

$$n_e\sqrt{l^2+d^2}-n_p l=(2m+1)\lambda/2, \tag{5.29}$$

where m is an integer, or

$$l[n_e\sqrt{1+(d/l)^2}-n_p]=(2m+1)\lambda/2, \tag{5.30}$$

then this interference is destructive. The odd number of half-wavelengths can be accumulated over many ducts. As shown in Fig. 5.9, the thicknesses of the ducts are on the order of a Debye length. After passing through all of the ducts, the ducted and unducted wavefronts merge and diffract as the beam propagates.

The threshold angle of incidence to achieve total internal reflection can be obtained from Snell's law,

$$\sin\theta_i=\frac{n_p}{n_e}, \tag{5.31}$$

and the grazing angle, $\theta_g=\pi/2-\theta_i$. Therefore, we can write Eq. 5.31 as

$$\cos\theta_g=\frac{n_p}{n_e}. \tag{5.32}$$

We can also write Eq. 5.32 as

$$\cos\theta_g=\frac{1}{\sqrt{1+\tan^2\theta_g}}=\frac{1}{\sqrt{1+(d/l)^2}}=\frac{n_p}{n_e}. \tag{5.33}$$

Therefore, we can solve Eq. 5.30, for l to obtain

$$l=\frac{n_p(2m+1)\lambda/2}{n_e^2-n_p^2}. \tag{5.34}$$

Equation 5.34 yields the accumulated distance that radiation must travel along multiple ducts for destructive interference to occur.

As we showed in Fig. 4.18, the maximum loss due to amplitude scintillations is 3 dB. Therefore, any larger fade is due to phase scintillations. Our model can explain the large fades that are grater than 3 dB that are observed in the peak power plot for DOY 115 in Fig. 4.3. The speed of the Mercury at aphelion is 38.7 km/s. So in order for the spacecraft that is moving around the Mercury to experience a fade that is one second long, the diffracted beam front has to be about 40 km wide.

Our model is also consistent with the fade depth statistics that were observed. For example, we may examine the 15 dB fade depth for DOY 344 in Fig. 4.10. Based on the data that we obtained for 374 fade occurrences of 15 dB or higher over 10800 seconds, a carrier suppression of 15 dB occurs within 10.2° of an odd multiple of $\pi/2$. Therefore, the probability of a fade for 15 dB is $10.2/360 = 0.028$. Our model predicts 302 events in this time period, which agrees well with the 374 fades that we observed in the data.

In order to obtain a good carrier-to-noise ratio, the receiver has a narrow loop filter, which in our case is about 60 Hz. If after phase modulation by the turbulence, carrier power is shifted to sidebands that lie outside the loop bandwidth, then the carrier is effectively suppressed, leading to a low carrier-to-noise ratio and a poor phase estimate. We have observed such carrier fading over a time scale of hundreds to thousands of seconds.

Ducting is a random process, and it varies in space and time due to physical processes in solar wind plasma that cannot be described in a deterministic way and must be characterized probabilistically, like atmospheric turbulence. However, at smaller SEP angles (less than 3°), the electron and proton densities are larger; so, the the difference in the index of refraction between the electron and proton plasma wave is larger. Therefore, the probability that ducts exist is larger. We are proposing that these ducts are responsible for the large fades that are observed in our data over a time scale of hundreds to thousands of seconds.

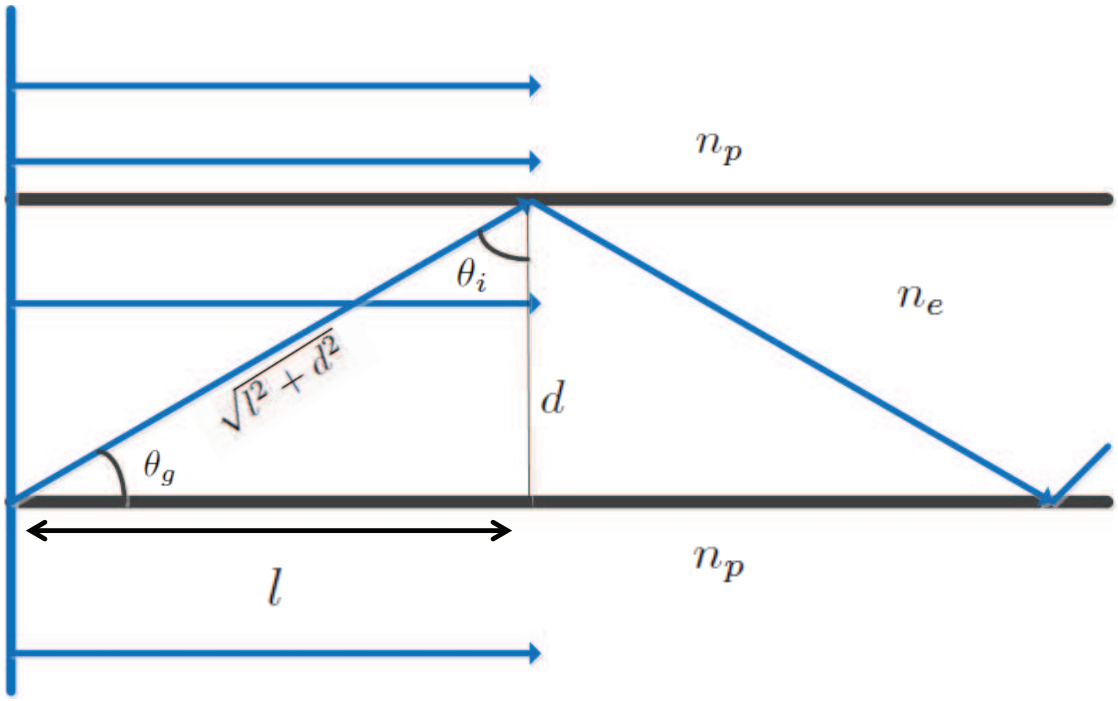

Figure 5.8: Schematic illustration of a portion of radiated plane wave that refracts into a duct because of the change in the refractive index, with a small grazing angle θ_g.

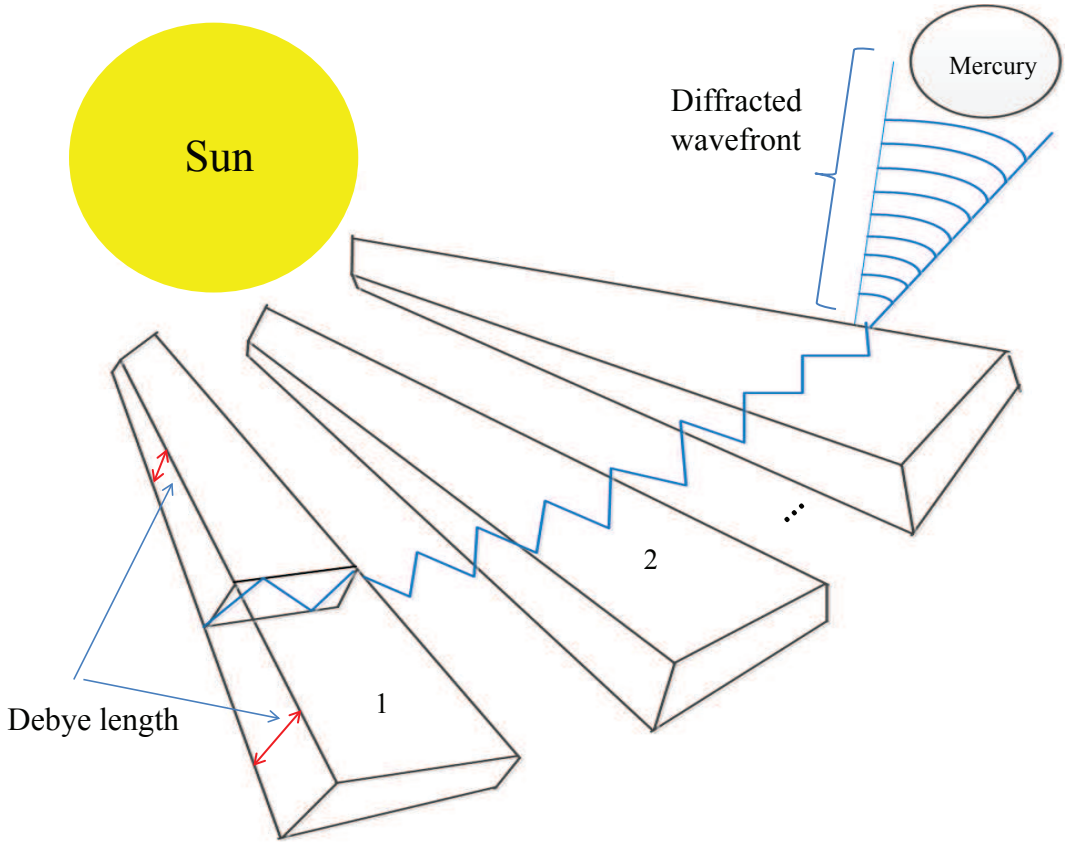

Figure 5.9: In order to reach Mercury an RF uplink beam can pass through many ducts. The thickness of the ducts are on the order of Debye length. After passing through all of the ducts, ducted and unducted wavefronts merge and diffract as the beam propagates.

Chapter 6

RF beam propagation simulation through solar plasma's turbulence

In this section of the dissertation, we present Monte Carlo simulations that reproduce the amplitude scintillations that we obtained from our data analysis. The scintillation index is a measure of the degree of fluctuation that a signal's amplitude experiences due to passage through turbulence. The definition of scintillation applies to any electromagnetic wave propagation through any turbulent medium. In the case that we study here, the RF wave scintillation is caused by scattering of the beam due to the refractive index irregularities that are related to the density fluctuations of the ions and the ducts. We will use the same phase screen method that is frequently used in optics to describe the amplitude scintillations that are due to plasma turbulence. We will use the Kolmogorov theory of turbulence in our simulations, as we have done in optical systems [(3) and (4), see Chapter 2].

We use the phase screen method to reproduce the scintillations. The starting point for our study is the paraxial wave equation [(1), Eq. 7.3],

$$2ik\frac{\partial U(\mathbf{R})}{\partial z} + \nabla_T^2 U(\mathbf{R}) + 2k^2 n_1(\mathbf{R})\, U(\mathbf{R}) = 0, \tag{6.1}$$

where $\mathbf{R} = (\mathbf{r}, z)$ is the position vector, r is the transverse distance, $\mathbf{r}$ is the corresponding

transverse vector, k is the angular wavenumber, ∇_T^2 is the transverse Laplacian operator, $U(\mathbf{R})$ is the envelope of the electric field, and $n_1(\mathbf{R})$ is the randomly fluctuating portion of the refractive indices of electron and protons. The solution of Eq. 6.1 over a small distance Δz can be written as

$$U(x,y,z+\Delta z) = U(x,y,z)\exp\left[ik\int_0^{\Delta z} dz' n_1\left(x,y,z'\right)\right]. \tag{6.2}$$

We then write the first two statistical moments of $\theta \equiv k\int_0^{\Delta z} dz' n_1(x,y,z')$,

$$\langle\theta\rangle = k\int_0^{\Delta z} dz' \langle n_1(x,y,z')\rangle = 0 \tag{6.3}$$

and

$$\langle\theta^2\rangle = k^2\int_0^{\Delta z} dz' \int_0^{\Delta z} dz'' \langle n_1(x,y,z') n_1(x,y,z'')\rangle. \tag{6.4}$$

Hence, we use $\langle . \rangle$ to denote the expected value, which we estimate by averaging over many realizations. We will use the method of randomly varying phase screens (3) and (4), combined with the split-step method (13), to calculate $U(\mathbf{r},z)$ for a particular realization, and from that we will calculate the scintillation index as the irradiance variance scaled by the square of the mean irradiance (1),

$$\sigma_I^2(\mathbf{r},z) = \frac{\langle I^2(\mathbf{r},z)\rangle}{\langle I(\mathbf{r},z)\rangle^2} - 1, \tag{6.5}$$

where the irradiance is $\langle I(\mathbf{r},z)\rangle = \langle U(\mathbf{r},z)\, U^*(\mathbf{r},z)\rangle$, and $U^*(\mathbf{r},z)$ denotes the complex conjugate field. The second moment of the irradiance is

$$\langle I^2(\mathbf{r},z)\rangle = \langle U(\mathbf{r},z)\, U^*(\mathbf{r},z)\, U(\mathbf{r},z)\, U^*(\mathbf{r},z)\rangle. \tag{6.6}$$

We averaged over 5000 realizations to obtain the expected values. This procedure is similar

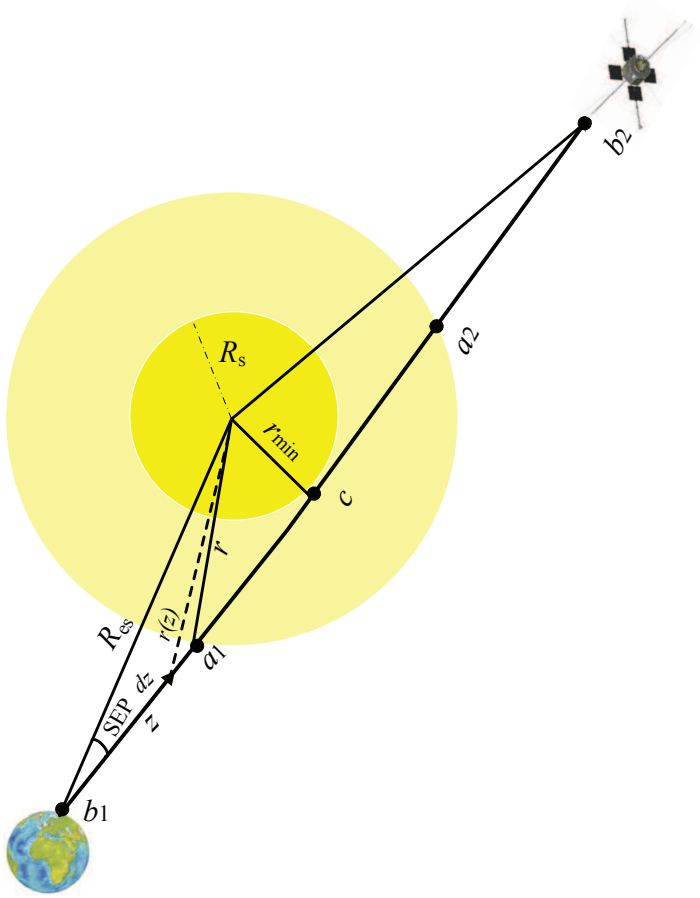

Figure 6.1: The simulation geometry.

to the procedure that we described in chapter 3, except that we are using a plane wave and not a Gaussian beam, since due to the long propagation distance the RF beam at the aperture is accurately approximated as a plane wave.

The geometry that we used is shown in Fig. 6.1, where

$R_s = 6.955 \times 10^8$ m, solar disk radius,

$r =$ solar corona radius, $100R_s$,

$z =$ the distance from Earth to the element dz in the signal path being integrated,

$R_{es} =$ distance from earth to Sun, 1.5×10^{11} m,

$r_{min} = R_{es} \sin(\text{SEP})$, the shortest distance from solar disk to the propagation path,

$b_1a_1 =$ distance from earth to where the turbulence media starts,

$b_1c = R_{\text{es}}\cos(\text{SEP})$, half of the total distance,

$b_1b_2 = 2 \times R_{\text{es}}\cos(\text{SEP})$, total propagation distance,

$a_1a_2 =$ the distance that the beam propagates in the turbulent medium,

$a_1c = \sqrt{r^2 - r_{\text{min}}^2}$,

$ca_2 = a_1c$,

$b_1a_1 = a_2b_2$,

$r(z) = \int_0^{a_1a_2} \left[R_{\text{es}}^2 + z^2 - 2zR_{\text{es}}\cos(\text{SEP})\right]^{1/2} dz$, and

C_n^2 may written as (23)

$$C_n^2 = a_1 \left[\frac{r(z)}{R_{\text{s}}}\right]^{-4} + b_1 \left[\frac{r(z)}{R_{\text{s}}}\right]^{-7}, \tag{6.7}$$

where a_1 and b_1 are fitting coefficients (23).

In Fig. 6.2, we compare the amplitude scintillations that we obtained from our Monte Carlo simulation to Morabito's result (23). As shown in the figure, our simulations predicts lower amplitude scintillations than does Morabito. We attribute this differences to bias in Morabito's result (23) from phase scintillations. We showed in Fig. 4.7 that the phase scintillations only occur when the rms phase deviation is an odd multiple of $\pi/2$, so that it is not always present.

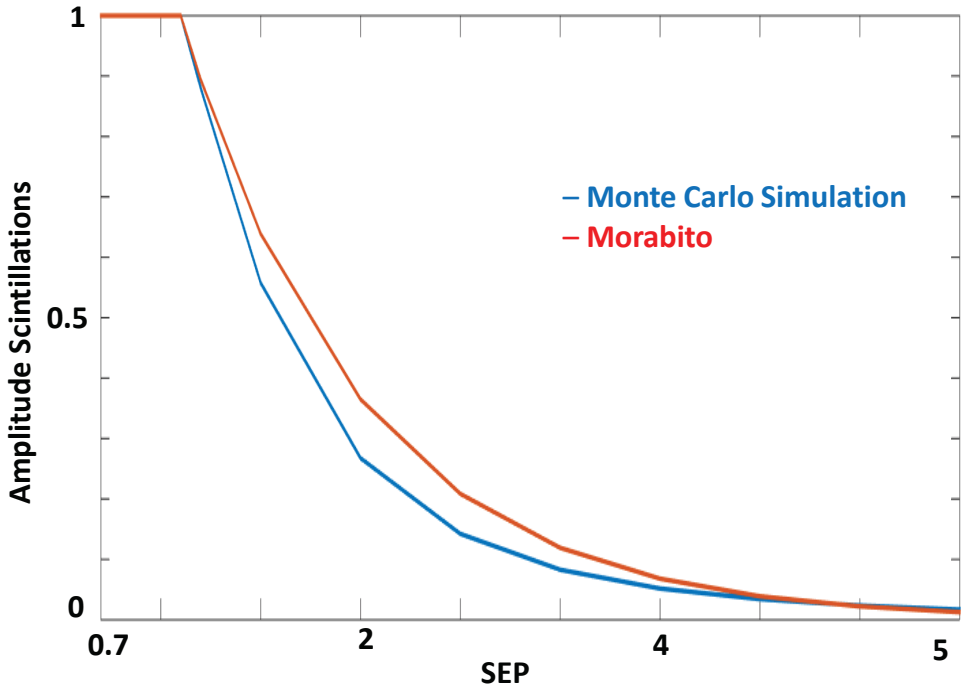

Figure 6.2: Amplitude scintillations from our Monte Carlo simulation compared to Morabito's result (22).

Chapter 7

Conclusion

In conclusion, we have studied the optical and RF beam propagation in turbulent media. For the optical beam, the turbulent medium was the atmosphere and for the RF beam it was the plasma in the solar corona. This research was broadly comprised of six separate projects. The first three projects focused on optical beam propagation through atmospheric turbulence and possible techniques to reduce optical scintillations at the receiver. The fourth and fifth projects were concentrated on the data analysis and theoretical study of RF beam propagation through the solar corona during planetary conjunction. The turbulence model that was used to study optical propagation was then applied to RF beam propagation to explain the amplitude scintillations that were observed in the data analysis and also to compare the impact of turbulence on optical and RF beam propagation.

In the first project, we obtained an analytical expressions for both the mean-square beam radius and the beam quality factor using the moment method that was first developed by Feizulin and Kravtsov (9). We have showed the moment method eliminates the need for knowledge of the turbulence structure function. Prior to our work there was no analytical expression for the spread of a laser beam and its degradation as it passes through atmospheric turbulence when there is an initial quartic aberration. Our expressions are valid for all distances, in contrast to the previous studies. We compared these expressions to the

results from Monte Carlo simulations, which allowed us to mutually validate the theory and our Monte Carlo codes. Also with simulations we showed the beam intensity follows a Gaussian-distribution for all distances as shown in Fig. 2.8. Additionally, we compared the simulation results to field test data. The agreement was excellent as shown in Fig. 2.5. In particular, we obtained good agreement between the scintillation index that is found experimentally and the scintillation index that is calculated in our simulations. We have shown that the probability distribution for the mean-square beam radius that the simulation predicts is a gamma-gamma distribution in agreement with experiments. Our results demonstrate the usefulness of Monte Carlo simulations as a way to both understand the experimental behavior and estimate the turbulence parameters.

We also used the Monte Carlo simulations to explain the discrepancy between a classic expression of Fante's for a Gaussian beam at a short distance of propagation versus using the result from the moment method. In the short-distance limit in which our result differed from Fante's, the beam radius was dominated by diffraction. So, the quantitative difference between the exact expression and Fante's relative to the total beam spread was small as shown in Fig. 2.7.

In the third project, we carried out simulations of partially spatially coherent infrared and visible (HeNe) laser beams with different degrees of spatial coherence as they propagate through a turbulent atmosphere. The results have been compared to both maritime and terrestrial field test data that were collected at the US Naval Academy. We compared the probability density function of the simulated intensity to what was observed in the field test data. The simulations predict a lognormal probability distribution function in agreement with experiments as shown in Figs. 3.3 and 3.4. We have shown that the scintillation index has possible sweet spots that are associated with specific degrees of partial spatial coherence of the laser beam and that depend on the propagation distance and atmospheric parameters as shown in tables 3.1 and 3.2. We obtained good agreement between the scin-

tillation index that is found experimentally and the scintillation index that is calculated in our simulations. We showed that partially coherent beams whose scintillation indices are lower than the index of a coherent beam are also less distorted by atmospheric turbulence.

In our fourth project, we analyzed recent data obtained during superior solar conjunction of MESSENGER spacecraft at X-band for days 114, 115, 339, 340, and 344 for year 2014 for an SEP angle between 0.7° and 1.84°. There have been prior studies of RF beam propagation during superior solar conjunction, but we obtained several new findings. Analysis of the data that was obtained over several MESSENGER conjunctions reveals a short-term and long-term effect. We showed that the amplitude scintillation imposed on the carrier signal is evident on a short-time scale. We also showed that the phase scintillation imposed on the carrier is stronger, and it occurs over a longer time duration. We also observed a non-monotonic behavior as the SEP angle changes. We have observed two distinct characteristics for the phase scintillation that is induced on the carrier, depending on whether the imposed phase modulation index is close to an odd multiple of $\pi/2$ or is far removed from it. The proximity to $\pi/2$ is related to carrier suppression. For example, when the phase modulation index is within 0.056 radians, a carrier suppression of 25 dB is expected; when the phase modulation is within 1.1 radians, a carrier suppression of 1 dB is expected as shown in Fig. 4.9. We have also obtained the phase scintillation spectral density, and we observed two distinct characteristics for it, depending on whether or not the carrier is suppressed. The phase scintillation spectral density for a non-carrier-suppressed condition is consistent with a Kolmogorov process for which the frequency dependence is proportional to $f^{-8/3}$, and this result is in agreement with prior investigations by Morabito (23) and Imamura (24) as shown in Fig. 4.12. When the carrier is suppressed, the receiver noise obscures the underlying turbulent process and produces instead an f^{-1} dependence, corresponding to the f^{-1} flicker noise of the receiver as shown in Fig. 4.13.

In our fifth project, we investigated possible explanations for the difference in time

scales between the amplitude and phase scintillations. Prior to our work, there was no physical explanation for why there are two different time scales for these observations. Our starting point was a study of the Sun's atmosphere and the plasma that surrounds it. We investigated four phenomena that exist in the solar wind that could potentially explain these long-time phase scintillations. We first investigated the propagation of radio waves in the positively and negatively charged clouds of protons and electrons that are approximately a Debye length in size. The difference between the indices of refraction in these clouds will lead to phase variations in the beam wavefront as an RF beam propagates. Second, we investigated the passage of supersonic particles through acoustic waves that locally change the index of refraction, leading to phase variation in the beam wavefront as an RF beam propagates. Third, we investigated the separation of electrons and protons that are due to inhomogeneous solar magnetic fields. This separation leads to local change in the indices of refraction and hence phase variation in the beam wavefront as an RF beam propagates. Fourth, we investigated ducts in solar plasma that trap a part of an RF beam, which leads to a phase difference in the beam wavefront as an RF beam propagates. We concluded that the most probable explanation for the difference in time scales between the amplitude and phase scintillations is the fourth, effect of long ducts. These ducts act as waveguides, changing the phase velocity of an RF beam as it travels along a zigzag path inside the duct. When the radiated wave exits from a duct, its phase is changed with respect to the signal that did not pass through the duct, which can lead to destructive interference and carrier suppression. The trapping of the wave is random in nature and can be either a fast or slow process. The predictions of this model are consistent with observations. Also our model explains the difference in time scales between the amplitude and phase scintillations.

Lastly, we showed since ducting is a random process, and it varies in space and time due to physical processes in solar wind plasma that cannot be described in a deterministic way and must be characterized probabilistically, like atmospheric turbulence, we can

characterize the solar wind turbulence as a Kolmogorov process. We used the same phase screen technique that was used to model optical propagation through turbulent atmosphere to simulate an RF beam as it propagates through the turbulent solar plasma. We reproduced the amplitude scintillations that we observed using Monte Carlo simulations. Our data and theoretical model were mutually consistent and indicate that solar plasma turbulence is a Kolmogorov process. Our Monte Carlo simulations confirmed this conclusion.

Reducing the scintillation at the receiver is one of the primary issues in free-space optical communication systems. We looked at a partially coherent beam technique with both IR (1550 nm) and HeNe (632.8 nm) lasers. We found a decrease in the scintillation compared to a fully coherent beam. In future work, it would be interesting to use different wavelengths and also different beam shapes, such as nonuniform polarized beam, which may lead to a significant scintillation reduction.

Our study of RF X-band propagation through the solar plasma will aid future missions that operate at or near solar conjunction to design communication links that can operate at SEP angles that are less than 3°. In future work, it would be interesting to also investigate how much improvement can be obtained by increasing the frequency, for example in the Ka-band, and compare the stability of links through the solar plasma.

References

[1] L. C. Andrews and R. L Phillips, *Laser Beam Propagation Through Random Media* (SPIE Press, Bellingham, WA, 2005).

[2] R. L. Fante, "Electromanetic beam propagation in turbulent media," Proc. IEEE **63**, 1669–1692 (1975).

[3] N. Mosavi, B. S. Marks, B. G. Boone, and C. R. Menyuk, "Optical beam spreading in the presence of both atmospheric turbulence and quartic aberration," in Free-Space Laser Communication and Atmospheric Propagation XXVI, H. Hemmati and D. M. Boroson, eds., Proc. SPIE **8971**, 897102 (2014).

[4] N. Mosavi, C. Nelson, B. S. Marks, B. G. Boone, and C. R. Menyuk, "Aberrated beam propagation through turbulence and comparison of Monte Carlo simulations to field test measurements," Opt. Eng. **53**, 086108 (2014).

[5] N. Mosavi, B. G. Boone, C. R. Menyuk, B. S. Marks, C. Nelson, J. R. Bruzzi , R. M. Sova, P. Malouf, K. B. Fielhauer, N. Adams, and B. H. Sequeira, "Strategies for Optimization of Deep Space Links: Selected Examples for Managing Propagation Path Loss," NASA SpaceOps workshop (2013).

[6] N. Mosavi, C. Nelson, B. S. Marks, B. G. Boone, and C. R. Menyuk, "Simulation of partially spatially coherent laser beam and comparison with field test data for both terrestrial and maritime environments," in Atmospheric Propagation XI, L. W. Thomas, E. Spillar, eds., Proc. SPIE **9080**, 908041 (2014).

[7] N. Mosavi, H. B. Sequeira, D. J. Copeland, D. M. Sepan, and C. R. Menyuk, "MESSENGER Solar Scintillation Measurements at Superior Solar Conjunction," in Nav-

igation and Communication Systems for Exploration, IEEE Aerospace Conference (2015).

[8] N. Mosavi, H. B. Sequeira, D. J. Copeland, and C. R. Menyuk, "Solar scintillation study during planetary conjunction," in Navigation and Communication Systems for Exploration, IEEE Aerospace Conference (2016).

[9] Z. I. Feizulin and Yu. A. Kravtsov, "Broadening of laser beam in a turbulent medium," Radiophys. Quantum Electron. **10**, 33–35 (1967).

[10] G. Gbur and E.Wolf, "Spreading of partially coherent beams in random media," J. Opt. Soc. Am. **19**, 1592−1598 (2002).

[11] A. E. Siegman, "Analysis of laser beam quality degradation caused by quartic phase aberrations," Appl. Opt. **32**, 5893−5901 (1993).

[12] A. E. Siegman and J. Ruff, "Effect of spherical aberration on laser beam quality," in *Laser Energy Distribution Profiles,* J. M. Darchuk, ed., Proc. SPIE **1834,** 130–139 (1992).

[13] T. Poon and T. Kim, *Engineering Optics With Matlab* (World Scientific Publishing Co., 2006).

[14] K. Petrowski, D. Limsui, C. Menyuk, R. Joseph, M. Thomas, and W. Torruellas, "Turbulent thermal blooming," in *Atomospheric Propagation V*, G. C. Gilbreath and L. M. Wasiczko, eds., Proc. SPIE **6951**, 695104 (2008).

[15] C. Nelson, S. Avramov-Zamurovic, R. Malek-Madani, O. Korotkova, R. Sova, and F. Davidson, "Measurements and comparison of the probability density and covariance functions of laser beam intensity fluctuations in a hot-air turbulence emulator with the maritime atmospheric environment," in *Laser Communication and Propagation*

through the Atmosphere and Oceans, A. M. J. van Eijk, C. C. Davis, S. M. Hammel, and A. K. Majumdar, eds., Proc. SPIE **8517**, 851707 (2012).

[16] J. C. Juarez, J. E. Sluz, C. Nelson, M. B. Airola, M. J. Fitch, D. W. Young, D. H. Terry, F. M. Davidson, J. R. Rottier, and R. M. Sova, "Free-space optical channel characterization in the maritime environment," in *Atmospheric Propagation VII*, L. M. Wasiczko Thomas and E. J. Spillar, eds., Proc. SPIE **7685**, 76850H (2010).

[17] C. Nelson, S. Avramov-Zamurovic, R. Malek-Madani, O. Korotkova, R. Sova, and F. Davidson, "Probability density function computations for power-in-bucket and power-in-fiber measurements of an infrared laser beam propagating in the maritime environment," in *Atmospheric Propagation VIII*, L. M. Wasiczko Thomas and E. J. Spillar, eds., Proc. SPIE **8038**, 80380G (2011).

[18] C. Nelson, S. Avramov-Zamurovic, O. Korotkova, R. Malek-Madani, R. Sova, and F. Davidson, "Probability density functions of power-in-bucket and power-in-fiber for an infrared laser beam propagating in the maritime environment," Appl. Opt. **52**, 7449−7461 (2013).

[19] V. A. Banach, V. M. Buldakov, and V. L. Mironov, "Intensity fluctuations of a partially coherent light beam in a turbulent atmosphere," Opt. Spektrosk. **54**, 1054−1059 (1983).

[20] J. C. Ricklin, and F. M. Davidson, "Atmospheric optical communication with a Gaussian Schell beam," J. Opt. Soc. Am. A **20**, 856−866 (2003).

[21] T. Shirai, O. Korotkova, and E. Wolf, "A method of generating electromagnetic Gaussian Schell-model beams," J. Opt. A: Pure Appl. Opt. **7**, 232–237 (2005).

[22] C. Nelson, S. Avramov-Zamurovica, O. Korotkovab, R. Malek-Madania, R. Sovac, and F. Davidson, "Measurements of partially spatially coherent laser beam intensity fluctuations propagating through a hot-air turbulence emulator and comparison with both terrestrial and maritime environments," in *Free-Space Laser Communication and Atmospheric Propagation XXV*, H. Hemmati and D. M. Boroson, eds., Proc. SPIE **8610**, 86100T (2013).

[23] D. D. Morabito, "Spectral broadening and phase scintillation measurments using interplanetary spacecraft radio links during the peak of solar cycle 23," Radio Science, **44**, RS6004, December 2009.

[24] T. Imamura, K. Noguchi, A. Nabatov, K.I. Oyama, Z. Yamamoto and M. Tokumaru, "Phase scintillation observation during coronal sounding experiments with NOZOMI spacecraft," Astronomy and Astrophysics **439**, 1165−1169 (2005).

[25] B. P. Lathi, *Modern Digital and Analog Commuunication Systems* (Oxford University Press, 1998).

[26] Large Angle and Spectrometric Coronagraph Experiment (LASCO) http://lasco-www.nrl.navy.mil/index.php, download date April 24 2015.

[27] A. Hanslmeier, *The Sun and Space Weather* (Springer, 2007).

[28] F. F. Chen, *Plasma Physics and Controlled Fusion* (A Division of Plenum Publishing Co., 1984).

[29] R. W. Schunk and A. F. Nagy, *Ionospheres* (Cambridge University Press, 2000).

[30] E. Marsch "Kinetic Physics of the Solar Corona and Solar Wind," Living Rev. Solar Physics **3**, 1 (2006).

[31] M. Maksimovic, I. Zouganelis, J. Y. Chaufray, K. Issautier, E. E. Scime, J. E. Littleton, E. Marsch, D. J. McComas, C. Salem, R. P. Lin, and H. Elliott "Radial evolution of the electron distribution functions in the fast solar wind between 0.3 and 1.5 AU," J. Geophys. Res. **110**, A09104 (2005).

[32] J. W. Chamberlain and D. M. Hunten, *Theory of planetary atmposheres* (Academic Press. 1987).

[33] National Science Foundation *"Magnetic Field Uses Sound Waves To Ignite Sun's Ring Of Fire."* Science Daily, 29 May 2007.

[34] N. Hershkowitz and Y. C. Ghim, "Probing plasmas with ion acoustic waves," Plasma Sources Sci. **18**, 014018 (2009).

[35] I. G. Hernandez, R. Komm, A. Pevtsov, and J. Leibacher, *Solar Origins of Space Weather and Space Climate* (Springer, 2014).

[36] E. Talebian and M. Talebian, "A general review on the derivation of ClausiusMossotti relation," Optik-International Journal for Light and Electro-Optics **124**, 2324−2326 (2013).

[37] D. E. Kerr, *Propagation of Short Radio Waves* (Peter Peregrinus, London, 1987).

[38] M. Grabner, V. Kvicera, and V. Zhurbenko (eds.) *Atmospheric Refraction and Propagation in Lower Troposphere, Electromagnetic Waves* (InTech, 2011).

[39] M. E. Thomas, *Optical Propagation in Linear Media: Atmospheric Gases and Particles, Solid-State Components, and Water* (Oxford University Press, 2006).